

Engineering of phenylpyridine- and bipyridine-based covalent organic frameworks for the photocatalytic tandem aerobic oxidation/Povarov cyclization.

Maarten Debruyne,^a Sander Borgmans,^b Sambhu Radhakrishnan,^c Eric Breynaert,^c Henk Vrielinck,^d Karen Leus,^e Andreas Laemont,^f Juul De Vos,^b Kuber Singh Rawat,^b Siebe Vanlommel,^b Hannes Rijckaert,^f Hadi Salemi,^a Jonas Everaert,^a Flore Vanden Bussche,^{a,f} Dirk Poelman,^d Rino Morent,^e Nathalie De Geyter,^e Pascal Van Der Voort,^f Veronique Van Speybroeck,^b Christian V. Stevens.*^a

^a Department of Green Chemistry and Technology, Ghent University. Coupure Links 653, 9000 Ghent.

^b Department of Applied Physics, Ghent University. Technologiepark 46, 9052, Zwijnaarde, Belgium.

^c NMR/X-ray platform for Convergence Research (NMRCoRe) & Centre for Surface Chemistry and Catalysis: Characterisation and Application Team (COK-KAT), KU Leuven, Celestijnenlaan 200f - box 2461, 3001 Leuven, Belgium.

^d Department of Solid State Sciences, Ghent University, Krijgslaan 281 (S1), 9000 Ghent, Belgium.

^e Department of Applied Physics, Faculty of Engineering and Architecture, Ghent University, Sint-Pietersnieuwstraat 41 (B4), 9000 Ghent, Belgium.

^f Department of Chemistry, Ghent University. Krijgslaan 281 (S3), 9000, Ghent, Belgium.

E-mail: Chris.Stevens@UGent.be

ABSTRACT

Covalent organic frameworks (COFs) are emerging as a new class of photoactive organic semiconductors, which possess crystalline ordered structures and high surface areas. COFs can be tailor-made towards specific (photocatalytic) applications and the size and position of their band gaps can be tuned by the choice of building blocks and linkages. However, many types of building blocks are still unexplored as photocatalytic moieties and the scope of reactions photocatalyzed by COFs remains quite limited. In this work, we report the synthesis and application of two bipyridine- or phenylpyridine-based COFs: **TpBpyCOF** and **TpPpyCOF**. Due to their good photocatalytic properties both materials were applied as metal-free photocatalysts for the tandem aerobic oxidation/Povarov cyclization and α -oxidation of *N*-aryl glycine derivatives, with the bipyridine based **TpBpyCOF** exhibiting the highest activity. By expanding the range of reactions that can be photocatalyzed by COFs this work paves the way towards the more widespread application of COFs as metal-free heterogeneous photocatalysts, as a convenient alternative for commonly used homogeneous (metal-based) photocatalysts.

Keywords: Covalent Organic Frameworks, photocatalysis, oxidation, Povarov reaction

INTRODUCTION

A booming world population and economy puts an ever-increasing pressure on the environment. Together with growing concerns about pollution, global warming, and the finite supply of fossil resources, this has led to the development of many different green technologies. One promising avenue is visible light photocatalysis, which utilizes the energy of visible light and converts it into chemical energy for organic reactions through a catalyst.¹⁻⁴ Based on whether the photocatalyst and the reactants exist in the same phase or not, it is classified as a homogeneous or heterogeneous photocatalyst, respectively. Typical examples of the former include metal complexes (mainly ruthenium and iridium complexes)^{5,6} and organic dyes (fluorenone, acridinium-based photocatalysts, xanthene dyes, etc.),⁷⁻¹⁰ whereas the latter category mainly contains inorganic semiconductors (TiO₂, CdSe, WO₃, ZnS, ZnO, etc.).¹¹⁻¹⁵ However, homogeneous catalysts, and especially the precious metal-based ones, have drawbacks such as high costs, difficult separation from the product, and low or no recyclability.

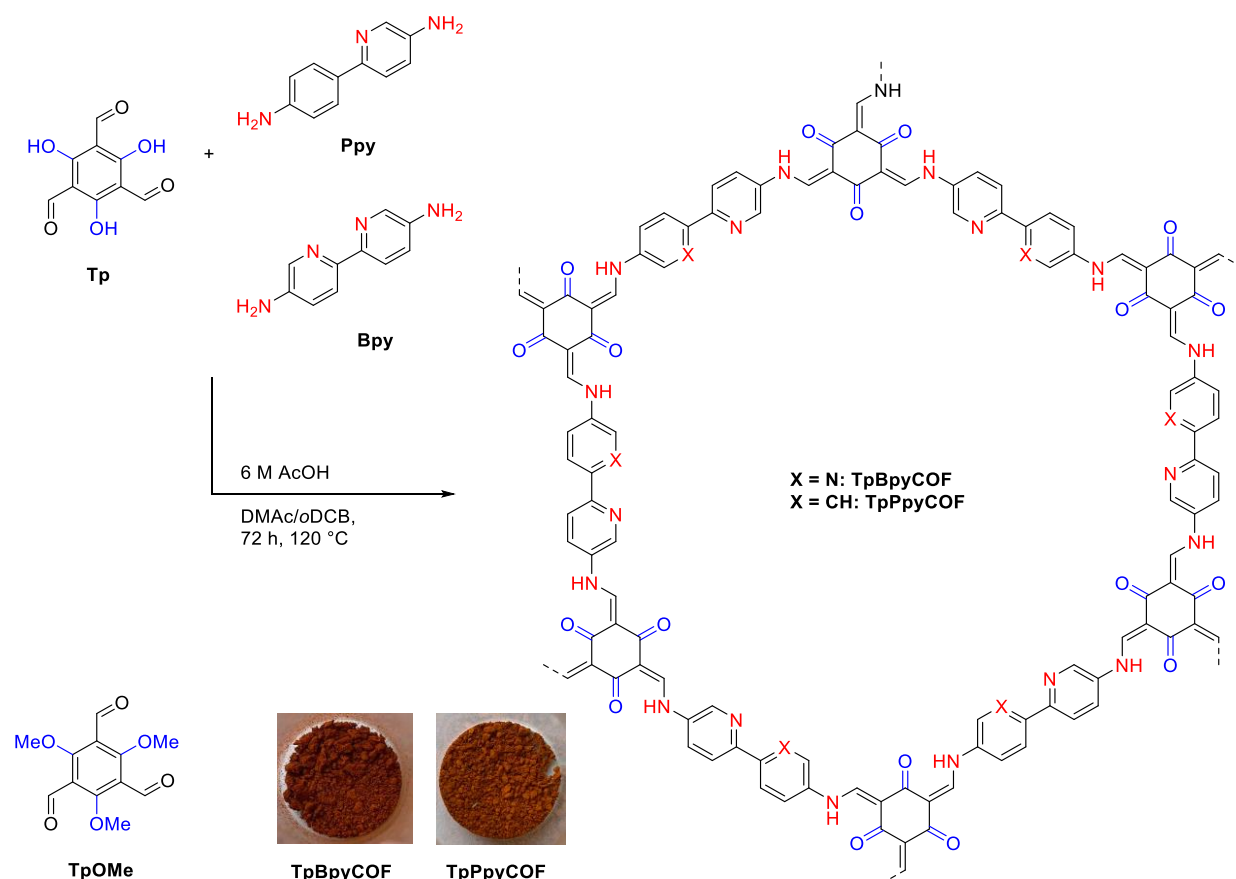
In recent years, new, heterogeneous, polymer-based photocatalysts such as graphitic carbon nitride (g-C₃N₄),^{16,17} metal organic frameworks (MOFs),^{18,19} and porous organic polymers (POPs)² have emerged to help eliminate these aforementioned deficiencies. Covalent organic frameworks (COFs) are a subclass of POPs, and like POPs, they are constructed completely from organic building blocks. Their defining characteristic is their long-range order and accompanying crystallinity. Due to their low weight, high specific surface area, and modular design, they have found application in diverse fields, such as gas sorption and separation,^{20,21} energy storage,^{22,23} sensing²⁴⁻²⁶ and heterogeneous catalysis.²⁷⁻³⁰ COFs hold a lot of promise as heterogeneous photocatalysts, with great recyclability due to their insolubility. Their extended π -conjugated frameworks, regular pore structures, and high surface areas are beneficial for obtaining high photocatalytic activities due to the good light absorbing capacity and high accessibility of their active sites.³¹⁻³³ Due to their tailor-made character, the optical properties and photocatalytic efficiency of COFs can be easily adjusted by the choice of building blocks.³⁴⁻³⁶ Nitrogen-rich moieties, when incorporated in extended frameworks, are known to confer significant photocatalytic activity. Whilst nitrogen-rich motifs such as triazines,^{33,37-39} porphyrins⁴⁰⁻⁴² and benzothiadiazoles⁴³⁻⁴⁶ have been applied extensively in metal-free heterogeneous photocatalysts, bipyridines and especially phenylpyridines have been less explored. Moreover, despite the advantages and the great amount of research currently being done on COFs as photocatalysts, the scope of reactions that are catalyzed by photoactive COFs is still quite limited. Mainly three reactions are studied: the aerobic oxidation of benzylamines, the hydroxylation of aryl boronic acids and the oxidation of sulfides. To expand this scope, we envisaged that the oxidation and subsequent transformations of *N*-aryl glycine derivatives would be feasible with COFs.

Herein, we describe the synthesis of two bipyridine- or phenylpyridine-based COFs: **TpBpyCOF** and **TpPpyCOF** and their application as photocatalysts. To evaluate their efficacy, we applied these materials in the COF- and Lewis acid-catalyzed photocatalytic aerobic oxidation/Povarov cyclization, allowing for the easy synthesis of highly substituted quinolines. Moreover, the same substrates could be converted into α -dicarbonyl compounds, when the Lewis acid was omitted. The results described in this work broaden the scope of COF-catalyzed photocatalytic reactions and thus facilitate the advancement of these emerging materials as alternatives for homogeneous (metal-based) catalysts.

RESULTS AND DISCUSSION

Synthesis and characterization of COFs

Two-dimensional (2D) COFs with one-dimensional open channels were synthesized by condensing 2,2'-bipyridine-5,5'-diamine (**Bpy**) or 6-(4-aminophenyl)pyridin-3-amine (**Ppy**) with 1,3,5-triformylphloroglucinol (**Tp**) by solvothermal synthesis as shown in Scheme 1. **TpBpyCOF** is already well known in literature^{47–51} and has been applied as a proton conductive solid state electrolyte,⁴⁷ as a carrier material for palladium or cobalt to use as a heterogeneous catalyst for benzofuran synthesis⁴⁸ or for electrochemical water oxidation,⁴⁹ as a fluorescence sensing material,⁵⁰ and recently as a metal free photocatalyst for the production of hydrogen peroxide.⁵¹ The newly synthesized **TpPpyCOF** is the first COF synthesized using **Ppy** as a building block, and this material has potential, not only as a photocatalyst, but also as a platform to complex metals with its phenylpyridine moiety. Moreover, we improved the existing synthesis of **Ppy**, by employing a Suzuki coupling reaction followed by reduction (see SI, Section S1.4), instead of the four step approach used previously.^{52,53} Next to these materials, another COF was made by condensation of **Bpy** with 2,4,6-trimethoxybenzene-1,3,5-tricarbaldehyde (**TpOMe**), which is known to give imine-linked COFs with exceptional stability.⁵⁴ While this COF has already been reported, it was synthesized via a mechanochemical reaction.⁵⁴ Interestingly, during the acidic conditions of the solvothermal COF synthesis unexpected demethylation of this material took place, as signified by solid state NMR, and a COF was formed that corresponded with **TpBpyCOF** (see SI, Section S2.7).



Scheme 1: Schematic illustration of the synthesized COFs. When **TpOMe** was condensed with **Bpy** a material largely corresponding to **TpBpyCOF** was formed (see SI, section S2.7 for more details).

PXRD patterns of the synthesized materials indicated relatively sharp reflections (Figure 4a) pointing to a good crystallinity of the resulting COFs. The peaks around $2\theta = 4^\circ$ are assigned to the (100) plane and the smaller peak around 7° to the (200) plane. The broad peak around 25° corresponds to the (001) plane and originates from π - π stacking between the individual layers of the COF.^{55–57} SEM and TEM images of the COFs are shown in Figure 1a-b. **TpBpyCOF** and **TpPpyCOF** form large aggregates, with relatively rough surfaces. The TEM images (Figure 1b) show the crystalline honeycomb like structure. Bright-Field (BF) TEM images of **TpBpyCOF** and **TpPpyCOF** with their corresponding EDX elemental map of carbon, nitrogen, and oxygen demonstrate the uniform distributions of these atoms throughout the framework (Figure S11-13). The permanent porosity of the synthesized COFs was assessed by N_2 sorption measurements at 77 K (Figure 2b). The calculated Brunauer–Emmett–Teller (BET) surface area for **TpBpyCOF** and **TpPpyCOF** were 879 and 755 m^2/g , respectively. The resulting pore size distributions (PSDs) are given in Figure S1-2 and the pore diameters were 17.9 and 18.5 Å for **TpBpyCOF** and **TpPpyCOF**, respectively. The simulated PSDs are shown in Figure S40-41 and possess a similar mean pore diameter, but exhibit a much more narrow distribution than the experimental PSDs.

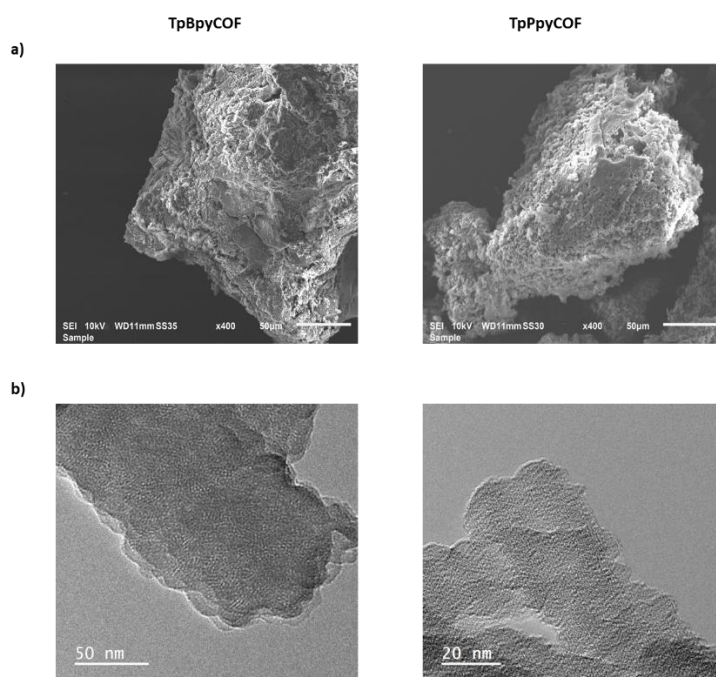


Figure 1: (a) SEM; and (b) TEM images of **TpBpyCOF** and **TpPpyCOF**.

Fourier transform infrared spectroscopy (FTIR) of these materials confirmed the completion of the reaction and the formation of β -ketoenamine linkages (Figure 2a and Figures S4-10). Disappearance of the characteristic absorption bands of the **Bpy** amino group ($3180\text{--}3418\text{ cm}^{-1}$) and the **Tp** carbonyl (1632 cm^{-1}) in the FTIR spectrum of **TpBpyCOF** points towards successful reaction. New peaks corresponding with the keto functionality are observed at 1604 (C=O) and $1564\text{ cm}^{-1}\text{ (C=C)}$.⁴⁷ The peaks around 1260 cm^{-1} correspond with the C–N bond.⁵⁰ For **TpPpyCOF**, similar results were obtained, the characteristic amine absorption bands ($3192\text{--}3443\text{ cm}^{-1}$) disappear and new bands corresponding with the C=O and C=C absorption, which are nearly merged in this material, appear around 1595 and 1568 cm^{-1} . For additional structural characterization, the N and C 1s XPS spectra were measured. The N 1s spectra of **TpBpyCOF** and **TpPpyCOF** are shown in Figure S14. The peaks at 398.8 and 398.5 eV for **TpBpyCOF** and **TpPpyCOF**, respectively, correspond to the C=N moieties (pyridinic nitrogens). The peak at 399.9 eV for both **TpBpyCOF** and **TpPpyCOF** correspond to the nitrogens of the enamine linkages (pyrrolic nitrogens). The N 1s spectrum of **TpBpyCOF** was deconvoluted in another smaller peak, at 401.2 eV, which was assigned to quaternary nitrogens, formed through side reactions or protonation.

The C 1s spectra of **TpBpyCOF** and **TpPpyCOF** were deconvoluted into three main peaks. One at 284.5 and 284.8 eV, for **TpBpyCOF** and **TpPpyCOF** respectively, corresponding to the C-C moieties, another at 285.6 and 286.0 eV corresponding to the C-N moieties, and a third peak at 287.9 and 288.3 eV corresponding to the carbonyl moieties.

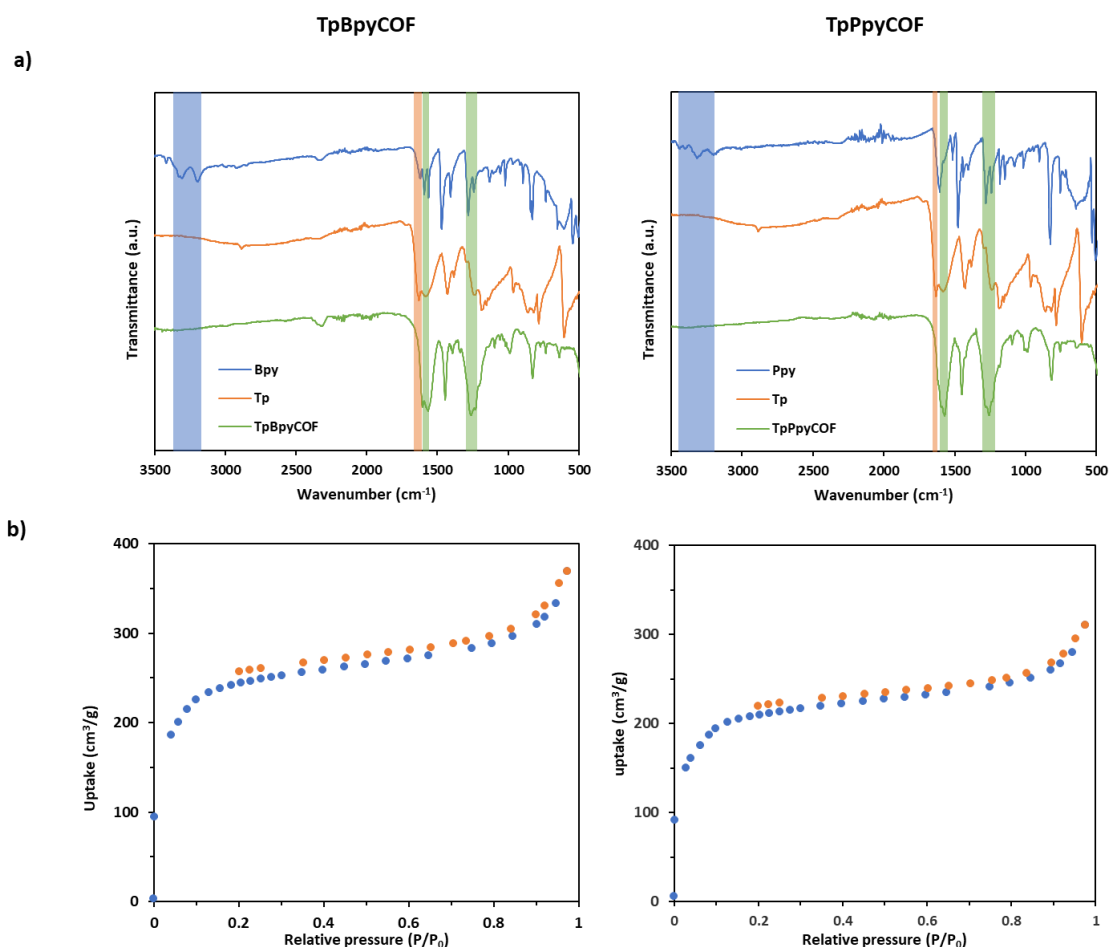


Figure 2: (a, left) Overlay of the FTIR spectra of **Bpy** (top, blue), **Tp** (middle, orange) and **TpBpyCOF** (bottom, green); (a, right) Overlay of the FTIR spectra of **Ppy** (top, blue), **Tp** (middle, orange) and **TpPpyCOF** (bottom, green). Characteristic signals originating from the amino groups, aldehydes and β-ketoenamine linkages are marked in blue, orange and green, respectively. (b) Nitrogen adsorption/desorption isotherms at 77K of **TpBpyCOF** and **TpPpyCOF**.

Multinuclear NMR spectroscopic studies were performed to obtain information about the local chemical structures of these materials. The ¹H MAS NMR spectra (Figure 2a-b and Figure S15) of the three COF's, **TpPpyCOF**, **TpBpyCOF** and '**TpOMeBpyCOF**', exhibited three broad resonances between 0-5 ppm, 5-10 ppm and 10-15 ppm. The resonance between 5-10 ppm is assigned to the aromatic and olefinic protons of the linker moieties, while the downfield shifted resonance between 10-15 ppm is attributed to the enamine ¹H. The upfield resonance between 0-5 ppm is not an expected resonance considering the ideal chemical structure, and could be attributed to the terminal -NH₂ groups or a composite resonance of strongly adsorbed water with the NH₂ terminals, strongly adsorbed solvents, etc. In the case of '**TpOMeBpyCOF**', the presence of the enamine ¹H resonance and the absence of the methoxy resonance in the ¹H-NMR spectrum (Figure S15) points towards an unexpected demethylation reaction during the COF synthesis. DQ-SQ NMR spectroscopy is a probe for the close spatial proximity between different nuclei (Figures 2g-h).^{58,59} The existence of correlations along the diagonal (autocorrelations) indicate the appearance as pairs for the respective nuclei and the appearance of off-diagonal correlations (cross correlations) at the sum of the respective frequencies

indicate their existence in close spatial proximity. The presence of the cross correlation (see Figures 2g-h, indicated as $\text{NH-H}_{\text{Ar/OI}}$) of the enamine resonance with the aromatic and olefinic ^1H 's indicate the successful linking between the **Tp** and **Bpy** or **Ppy** linkers in **TpBpyCOF** and **TpPpyCOF**, respectively. The cross correlation between the upfield ^1H resonance (0-5 ppm) and the aromatic/olefinic resonance (labelled as $\text{NH}_2\text{-H}_{\text{Ar/OI}}$) points towards its existence in the same phase and could be attributed to the existence of terminal NH_2 groups. The ^1H - ^{13}C CPMAS spectrum of all the COF samples exhibited the presence of carbonyl resonances around 185 ppm and multiple overlapping aromatic/olefinic ^{13}C resonances between 108-151 ppm (Figure S16). In line with the ^1H NMR spectrum, the methoxy resonances were absent in the case of '**TpOMeBpyCOF**', confirming its demethylation, and this material exhibited resonances similar to **TpBpyCOF**. The ^1H - ^{13}C CP-HETCOR spectra (Figure 3d,f) evidenced the correlation of the enamine ^1H resonance to the different ^{13}C nuclei in both the linkers, further confirming the local chemical structure. The correlations of the enamine resonance to the **Bpy** or **Ppy** linkers are depicted by the blue horizontal bar, while the correlation to the **Tp** linker is indicated by the yellow, green, & cyan horizontal bars. Modelling of the chemical shielding parameters (GIPAW VASP) was performed and the theoretically estimated chemical shifts are in perfect agreement with the experimental spectra for **TpBpyCOF** and **TpPpyCOF**, allowing assignment of all resonances and confirming the local chemical structure of these materials (SI, Section S3.6).

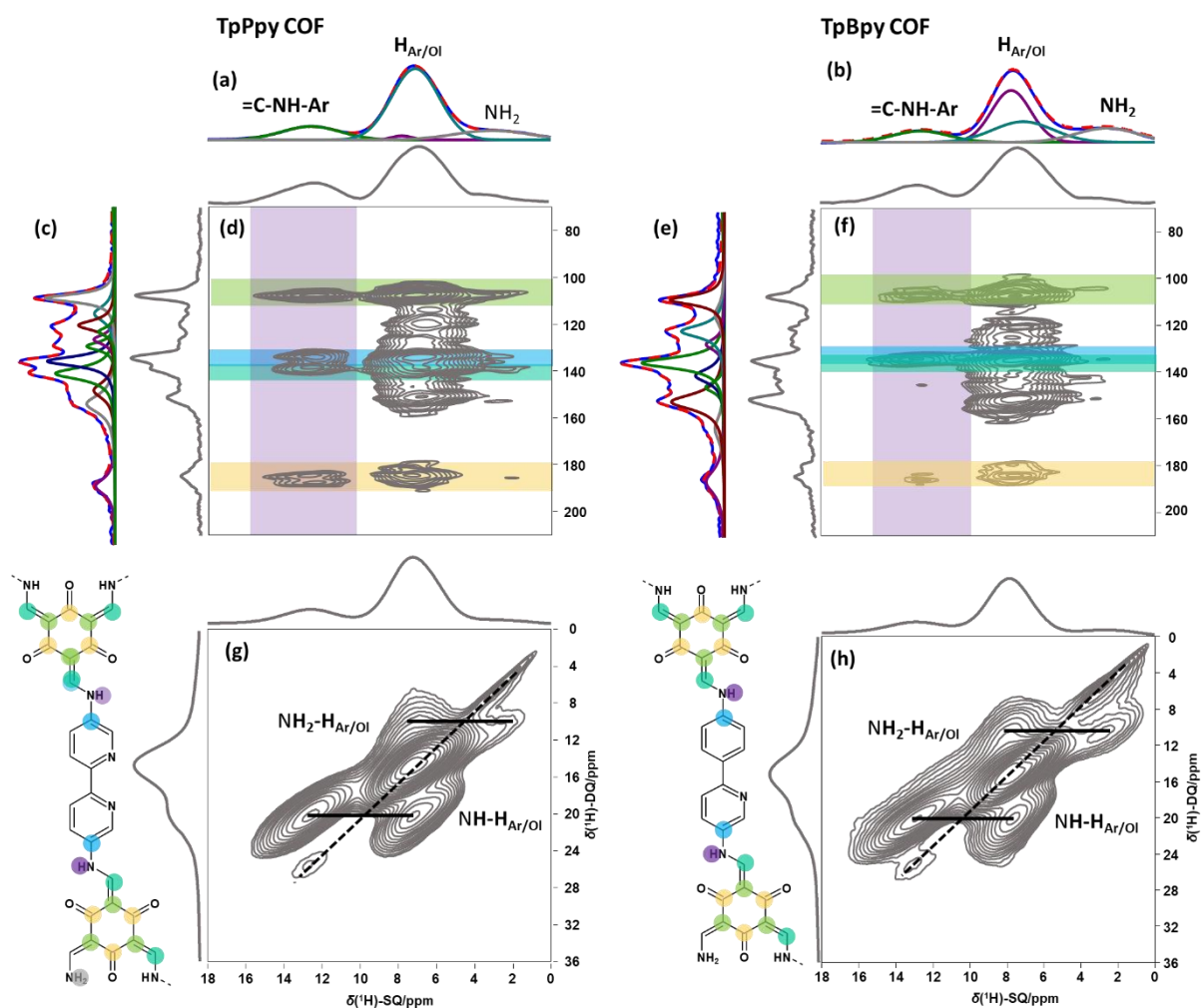


Figure 3: (a) and (b): ^1H direct excitation spectrum of **TpPpyCOF** and **TpBpyCOF**. (c) ^1H - ^{13}C CPMAS spectrum with spectral decomposition and (d) ^1H - ^{13}C CP-HETCOR spectrum of **TpPpyCOF**. (e) ^1H - ^{13}C CPMAS with spectral decomposition and (f) ^1H - ^{13}C CP-HETCOR spectrum of **TpBpyCOF**. (g) and (h) ^1H - ^1H DQ-SQ NMR spectra of **TpPpyCOF** and **TpBpyCOF**. All the spectra were acquired at 18.8 T under 35 kHz MAS at a sample temperature of 295 K.

The atomic structure of the materials was further determined through computational modelling (see Section S3), using the measured diffraction patterns as reference data. Through judicious comparison of the experimental diffraction patterns with a collection of calculated diffraction patterns, corresponding to different possible structure models, the most representative model was identified.⁶⁰ Moreover, by performing molecular dynamics (MD) simulations at operating conditions (1 bar, 300 K), peak broadening effects due to movement of the layers were effectively included in our calculated diffraction patterns for optimal comparison. The models were generated, starting from a hexagonal layer topology (**hcb**), combinatorically varying all flexible moieties in the layer geometry that might not be able to transition at operating conditions during the MD simulation, due to prohibitively large free energy barriers. Moreover, as typically only the nearest neighboring layer orientation is relevant due to screening effects, and to allow for different variations between subsequent layers, two-layer unit cells were constructed. The orientations of both the pyridine (py) moieties and the enamine linkages were considered (see Figure S32). The molecular interactions in these systems were modelled using system-specific force fields, derived using the QuickFF protocol (see section S3.1). Ultimately, this approach gave rise to a single optimal atomic structure for the materials, as visualized in Figure 4a, with excellent agreement to the experimental PXRDs. For **TpBppyCOF**, the optimal structural model has enamine linkages with an identical orientation in the same layer but inverted with respect to the layer above. The bipyridine is in a *trans* configuration and is inverted with respect to the layer above. For **TpPppyCOF**, the optimal structural model has enamine linkages with an identical orientation in the same layer but inverted with respect to the layer above. The pyridine unit is inverted with respect to the layer above and also switches position. The orientation of asymmetric moieties in COFs, such as the linkage and the configuration of bipyridine/phenylpyridine linkers are usually not modelled. However, by utilizing this methodology, we were able to obtain a more comprehensive understanding of these materials' configurations. Additionally, the good agreement observed between the modelled and experimental PXRDs provides evidence of the high crystallinity of these materials.

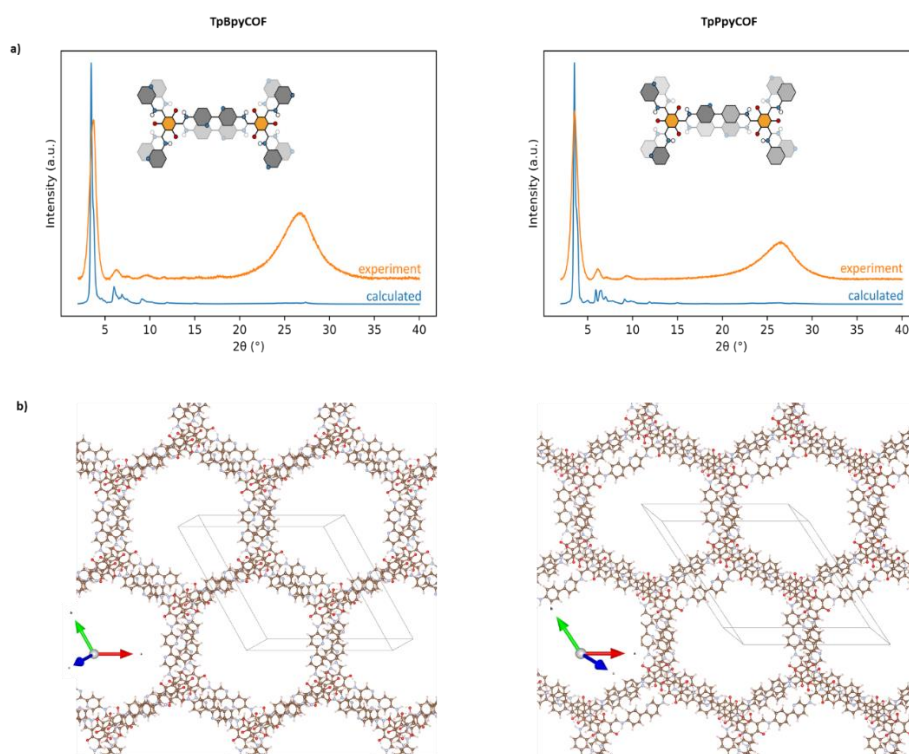


Figure 4: (a) PXRD comparison for **TpBppyCOF** and **TpPppyCOF** between experimental measurements and calculated MD averages. (b) Simulation derived structure for **TpBppyCOF** and **TpPppyCOF**.

Diffuse reflectance UV-Visible spectroscopy was performed to characterize the optical properties of the materials. The diffuse reflectance UV-Vis spectra of the COFs were measured and transformed through the Kubelka-Munk function to obtain the absorption spectra. These spectra exhibit absorption edges around 500 nm and the absorption tails extend beyond 850 nm (Figure 5a). It can be clearly seen that the absorption edge for **TpPpyCOF** is blue-shifted, compared to that of **TpBpyCOF**. The related Tauc plots (Figure 5b) were used to estimate the band gaps, which amounted to 2.10 and 2.23 eV for **TpBpyCOF** and **TpPpyCOF**, respectively, indicating that the substitution of a nitrogen atom in bipyridine to a carbon in phenylpyridine increased the band gap by 0.13 eV. The band gaps and density of states were calculated using the hybrid functional (HSE06) (Figure S35). The calculated band gaps were 2.09 and 2.14 eV for **TpBpyCOF** and **TpPpyCOF**, respectively, in good agreement with the experimental values. In both cases, the band gaps were quite small, allowing absorption of visible light and its conversion into useful chemical energy.

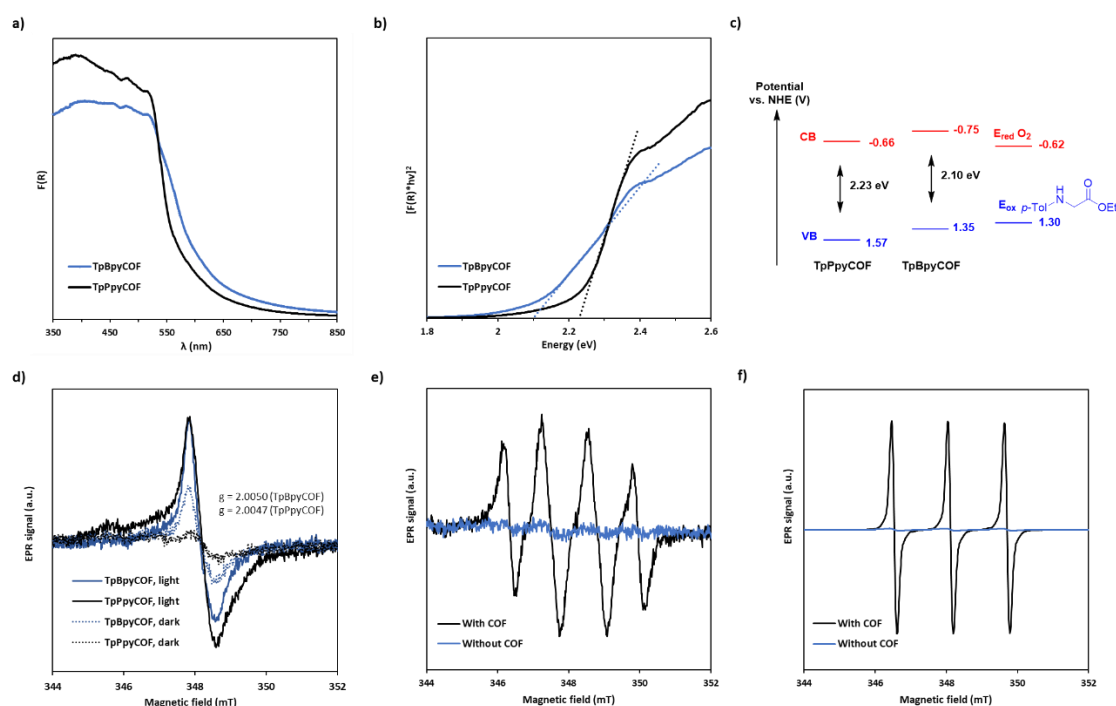


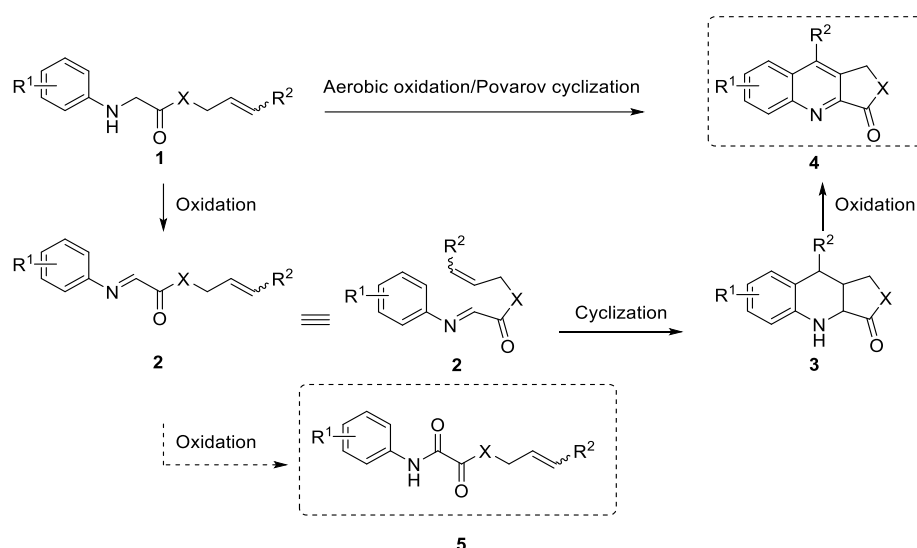
Figure 5: (a) Kubelka-Munk absorption spectra; (b) Tauc plots; (c) Band structure; (d) EPR spectra of **TpBpyCOF** and **TpPpyCOF**. (e) EPR spectrum of DMPO-OOH* and (f) TEMPO produced by **TpBpyCOF** under visible light irradiation.

Finally, the absolute positions of the valence band (VB) and conducting band (CB) of these COFs were estimated by linear sweep voltammetry under chopped light illumination.^{61,62} To this end, the COFs were mechanically exfoliated by grinding and coated on a working electrode. This was then used in a three-electrode setup, with an Ag/AgCl reference electrode and a Pt coil counter electrode. The anodic photocurrent was measured under chopped white light illumination and an applied bias which was swept from +0.4 V to -0.4 vs. Ag/AgCl. The resulting photocurrent decreased in magnitude and changed sign when going from +0.4 V to -0.4 V (Figure S16-17). The energy level of the conduction band can be determined from the potential at which this sign change occurs. The energy levels of the valence band can then be calculated using the equation: $E_{CB} = E_{VB} - E_g$ (Figure 5c).⁶³ To perform the targeted Povarov reaction, the amines of the glycine esters need to be oxidized and oxygen reduced. The reduction potential of O_2 is -0.62 V (vs. NHE)⁶⁴ and the oxidation potentials for a representative *N*-aryl glycine ester, ethyl *p*-tolylglycinate is 1.30 V (vs. NHE).⁶⁵ According to these potentials both COFs can reduce oxygen to the superoxide radical and both COFs are sufficiently oxidizing to accept electrons

from a representative *N*-aryl glycine ester. Next to these direct electron transfer reactions, these COFs could also act as photosensitizers to generate singlet oxygen. Singlet oxygen can be produced by semiconductors, such as COFs, through two main mechanisms. In a Dexter type energy transfer mechanism, one electron reduction of O₂ to O₂^{-•} takes place, followed by one electron oxidation. Alternatively, Förster resonance energy transfer allows the transfer of the energy of the excited state of the COF to oxygen, through dipole-dipole interactions between oxygen and the electric field produced by the separated charges.^{66,67} Singlet oxygen is a powerful oxidizing agent and can oxidize the desired substrates, hereby allowing the desired reactions to occur. By using EPR-spectroscopy and **TpBpyCOF** as the model catalyst, the ability of this material to create activated forms of oxygen (O₂^{-•} and ¹O₂) was confirmed. By stirring a suspension of the COF in acetonitrile with 5,5-dimethyl-1-pyrroline-*N*-oxide (DMPO), under air and visible light irradiation, the EPR spectrum of DMPO-OOH[•], generated by reaction between DMPO and photogenerated superoxide radicals, was detected (Figure 5e).⁶⁸ Using a similar methodology, with 2,2,6,6-tetramethylpiperidine (TEMP) as the spin trap, the production of singlet oxygen was demonstrated by the detection of the characteristic spectrum of the TEMPO free radical (Figure 5f). Moreover, both **TpBpyCOF** and **TpPpyCOF** gave EPR signals in the solid state that greatly increased under visible light illumination, signifying the photogeneration of electron-hole pairs (Figure 5d).⁶⁹

Tandem oxidation/Povarov cyclization

The prepared photocatalysts were applied towards the tandem aerobic oxidation/Povarov cyclization, which allows the synthesis of quinoline-fused lactones and lactams **4** from cinnamyl 2-(arylamino)-acetates and acetamides **1** (Scheme 2). Quinoline-fused lactones and lactams are an important class of heterocycles and also serve as synthons for the synthesis of natural products and analogues such as Uncialamycin,^{70–72} Luotonin A,⁷³ Camptothecin,⁷⁴ and quinolinecarboxamides^{75,76} (Figure S42). The first report on this transformation used difficult-to-synthesize glyoxal imines **2** as starting materials with BF₃·Et₂O as a Lewis acid to catalyze the cyclization and stoichiometric DDQ to oxidize the intermediary tetrahydroquinoline **3**.⁷⁰ However, *in situ* generation of the imines from the corresponding, easily accessible and stable amines **1** proved to be much easier and can be achieved by a stoichiometric oxidant such as Oxone.⁷⁷ Tris(4-bromophenyl)ammoniumyl hexachloroantimonate, a radical cation salt, has also been used catalytically for this reaction with air as the terminal oxidant,⁷⁸ however, it is a moisture-sensitive irritant.⁷⁹ Moreover, tris(bipyridine)ruthenium/BF₃·Et₂O⁸⁰ or rhodamine 6G/HClO₄⁸¹ have been used as a photocatalyst/acid couple for this transformation. Nevertheless, a metal-free heterogeneous photocatalyst has not yet been reported for this reaction, whilst it can give many advantages, such as easy separation and catalyst recovery, avoiding toxic and expensive metals.

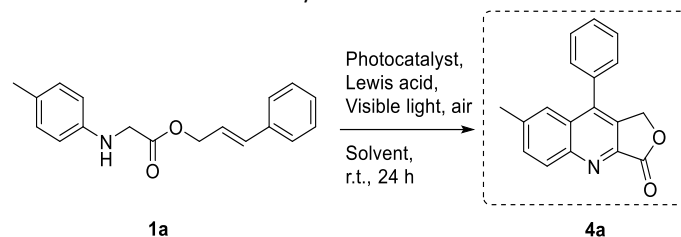


Scheme 2: One-pot oxidation-Povarov cyclization.

The initial reaction conditions, using 10 mol% BF₃·Et₂O in acetonitrile at room temperature and exposed to air, were chosen based on literature data⁸⁰ (Table 1, entry 1-2). This gave moderate yields of 38% and 32% for **TpBpyCOF** and **TpPpyCOF**, respectively. When no Lewis acid was used, the formation of a side product, cinnamyl 2-oxo-2-(*p*-tolylamino)acetate **7a**, was detected in 42% yield (Table 1, entry 5). To further optimize the yield and to avoid the moisture- and air-sensitive BF₃·Et₂O,⁸² many different Lewis and Brønsted acids were screened (Table 1, entry 6-30). First, the easier to handle and heterogeneous BF₃@silica was used, which also gave acceptable yields (Table 1, entry 6). However, Sc(OTf)₃ gave the most promising results (Table 1, entry 14). When higher or lower amounts than the standard 10 mol% were used, lower yields were obtained (Table 1, entry 31 and 32). The screening of other solvents than acetonitrile such as PhCF₃, EtOH, THF, CH₂Cl₂, DMF, HFIP, or 1,2-DCE (Table 1, entry 34-41) all resulted in lower yields, except for nitromethane which also gave promising results (Table 1, entry 41). Nitromethane was then also screened with some other Lewis acids (Table 1, entry 42-43), however, this did not improve the yields and finally CH₃CN was chosen because it is much less harmful than CH₃NO₂. Lastly, **TpPpyCOF** was again tested using Sc(OTf)₃, as well as Ru(Bpy)₃(PF₆)₂ and both gave worse results than **TpBpyCOF** (Table 1, entry 44-46). While **TpBpyCOF** and **TpPpyCOF** possess very similar surface area and optical properties, **TpBpyCOF** does show higher yields. It is likely that

TpBpyCOF's energy levels are more suited for singlet oxygen activation, hereby enhancing the catalytic activity.

Table 1: Optimization of the tandem oxidation-Povarov cyclization.^a



Entry	Photocatalyst	Lewis acid	Solvent	Yield (%) ^b
1	TpBpyCOF	BF ₃ ·Et ₂ O	CH ₃ CN	38
2	TpPpyCOF			32
3	[Ru(Bpy) ₃](PF ₆) ₂ ^c			22
4	[Ru(Bpy) ₃](PF ₆) ₂ ^d			43
5	TpBpyCOF	No Lewis acid		/ ^e
6	TpBpyCOF	BF ₃ @SiO ₂		48
7		1 eq. BF ₃ ·Et ₂ O		26
8		BF ₃ ·Et ₂ O/TMSOTf		46
9		TMSOTf		55
10		Cu(OTf) ₂		19
11		Bi(OTf) ₃		38
12		TFA		41
13		Dy(OTf) ₃		52
14		Sc(OTf)₃		61
15		HN(OTf) ₂		45
16		Zn(OTf) ₂		29
17		AlCl ₃		25
18		Ho(OTf) ₃		36
19		Yb(OTf) ₃		49
20		Er(OTf) ₃		40
21		La(OTf) ₃		41
22		Sm(OTf) ₃		49
23		Eu(OTf) ₃		45
24		HAuCl ₄ ·3H ₂ O		33
25		Gd(OTf) ₃		40
26		In(OTf) ₃		40
27		Ce(OTf) ₃		57
28		CeCl ₃ ·7H ₂ O		20
29		TiCl ₄ ·2THF		9
30		B(PhF ₅) ₃		14
31		5 mol % Sc(OTf) ₃		32
32		30 mol % Sc(OTf) ₃		39
33		10 mol % Sc(OTf) ₃	CH ₃ CN ^f	52
34			PhCF ₃	27
35			EtOH	5
36			THF	17
37			CH ₂ Cl ₂	22
38			DMF	12
39			1,2-DCE	32
40			HFIP	n.r. ^g
41			CH ₃ NO ₂	60
42		TMSOTf	CH ₃ NO ₂	57
43		B(PhF ₅) ₃	CH ₃ NO ₂	26
44	TpPpyCOF	Sc(OTf) ₃	CH ₃ CN	49
45	[Ru(Bpy) ₃](PF ₆) ₂ ^c			12
46	[Ru(Bpy) ₃](PF ₆) ₂ ^d			42

^a Reaction conditions: 0.1 mmol cinnamyl *p*-tolylglycinate **1a**, COF (10 mg) or [Ru(Bpy)₃](PF₆)₂ (1 or 10 mol%),^{c,d} 10 mol% Lewis acid, 1 mL CH₃CN, 26 W CFL, 24 h, r.t.

^b Determined by ¹H-NMR analysis using 1,3,5-trimethoxybenzene or mesitylene as an internal standard.

^c 1 mol%.

^d 10 mol%.

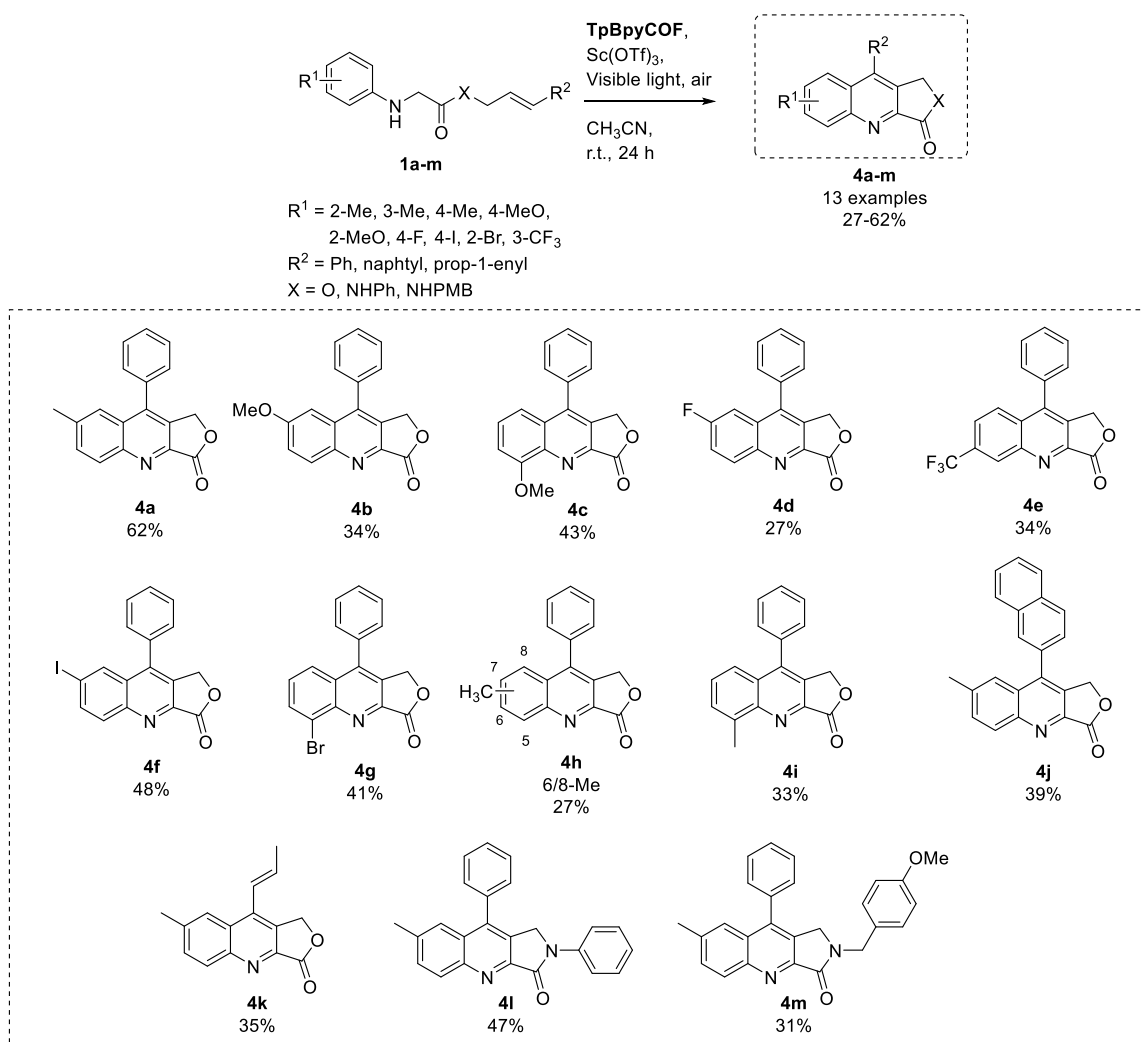
^e 42% cinnamyl 2-oxo-2-(*p*-tolylamino)acetate **7a** was detected.

^f 5 mL CH₃CN.

^g No reaction.

With the optimal conditions at hand, the scope of the reaction was examined by reacting a wide range of substrates **1a-m** with both electron-withdrawing (F, CF₃, Br, I) and electron-donating (OMe, Me) substituents in various positions (*ortho*-, *meta*- and *para*-). The corresponding quinolines **4a-m** were obtained in moderate yields (27-62%, Table 2). While full conversion of the starting materials was achieved in any case, side reactions and losses during isolation resulted in moderate isolated yields. As major side products were generally not observed in ¹H-NMR and LC-MS analysis, it is thought that the substrates partly polymerize during the reaction to form insoluble oligomers, which lower the yield. When using *meta*-substituted aryls, mixtures of the 6- and 8-substituted regioisomers were observed, of which only the isomer **4e** could be isolated in the case of the trifluoromethyl substituted quinoline. Substitution of the R²-group was also tolerated and both naphthalene and vinylene substituted quinolines **4j** and **4k** could be isolated with acceptable yields (39% and 35%). The photochemical synthesis of quinoline fused lactams had not yet been reported, and to our delight quinoline fused lactams **4l-m** could also be synthesized and isolated in 47% and 31% yield.

Table 2: TpBpyCOF and Sc(OTf)₃ catalyzed synthesis of quinolines **4a-m**.^{a,b}



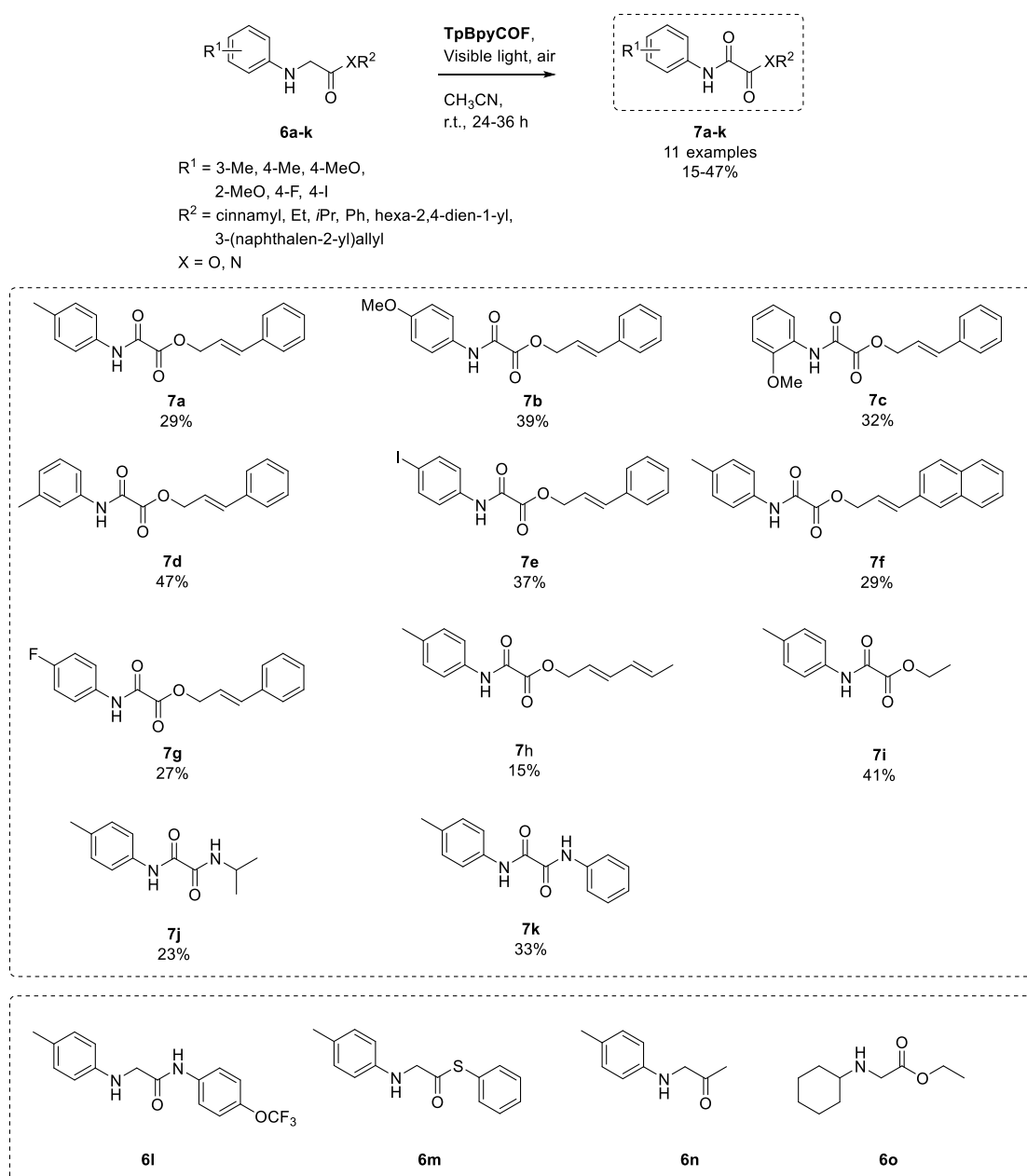
^a Reaction conditions: 0.2 mmol substrate **1**, 20 mg TpBpyCOF, 0.02 mmol Sc(OTf)₃, 2 mL CH₃CN, 26 W CFL, 24 h, r.t.

^b Isolated yields are reported.

Next to these quinolines, a series of oxalic acid derivatives **7a-k** could be synthesized by photocatalytic α -oxidation of the glycine derivatives **6a-k** when no Lewis acid was present in the system (Table 3). For the α -oxidation of *N*-aryl glycine derivatives there had only been incidental reports of the occurrence of the α -dicarbonyl compounds as side products during photocatalytic reactions.⁸⁰ To the best of our

knowledge, **TpBpyCOF** is the first photocatalyst used (homogeneous or heterogeneous) to study this reaction in more detail and examine the substrate scope. A wide range of oxalic acid derivatives **7a-k** could be produced using **TpBpyCOF**, albeit in relatively low isolated yields (15-47%). These rather low yields were due to side reactions and losses by purification using reversed phase chromatography. For the trifluoromethoxy-substituted substrate **6l**, no product could be isolated, due to the low stability of the starting material in solution. For thioester **6m**, the oxidized end product was obtained, however, it could not be fully separated from impurities. The product resulting from oxidation of ketone **6n** was obtained in only a very low yield (6%). For compound **6o** no product was obtained, and degradation of the COF was observed as the nucleophilic amine attacks the β -ketoenamine linkage and solubilizes the COF.

Table 3: COF catalyzed synthesis of oxalic acid derivatives **6**.^{a,b}



^a Reaction conditions: 0.2 mmol substrate **6**, 20 mg **TpBpyCOF**, 2 mL CH_3CN , 26 W CFL, 24-36 h, r.t.

^b Isolated yields are reported.

To probe the mechanism of the oxidation/Povarov cyclization, several control experiments were performed. In the dark, under argon or without COF, no product was formed (Table 4, entry 2-4). In absence of a Lewis acid the oxalic acid derivative was formed (Table 4, entry 5). Thus oxygen, light, the COF and the Lewis acid were essential for the transformation. As proven by the EPR experiments (Figure 5e-f), **TpBpyCOF** is capable of photogenerating both superoxide radicals and singlet oxygen, and both these pathways could be feasible to generate the products. To study the role of oxygen, several quenchers were added (Table 4, entry 6-14). Using quenchers for the superoxide radical, *p*-benzoquinone⁸³ or nitro blue tetrazolium chloride,⁸⁴ only a slight decrease in yield was observed. Similarly, *i*PrOH, a quencher for hydroxyl radicals,⁸⁵ did not lower the yield significantly. However, when using quenchers for singlet oxygen, such as L-histidine,⁸⁶ DABCO⁸⁷ or sodium azide⁸⁸ the reaction was inhibited effectively. This leads us to conclude that the key driver for this transformation is singlet oxygen. When quenching holes and electrons using KI⁸⁹ and AgNO₃⁹⁰, respectively, the yield was also lowered. In the presence of TEMPO⁹¹, a known radical scavenger, the yield lowered drastically (Table 4, entry 14), suggesting the involvement of radical processes. Based on these control experiments and previous reports^{77,80,92} we propose the following mechanism (Scheme 3). Upon irradiation of the COF, singlet oxygen is produced by direct energy transfer⁹³⁻⁹⁷ or by sequential oxidation/reduction of molecular oxygen.⁹⁸ The photogenerated singlet oxygen then oxidizes the amine **1** to the corresponding imine **2**, hereby generating H₂O₂.⁹⁹⁻¹⁰¹ The crude NMR spectra (Figure S43) clearly indicate the production of hydrogen peroxide, which is present in an approximately one-to-one ratio with the product **4**. In absence of a Lewis acid imine **2** is further oxidized to the oxalic derivative **5**. In presence of a Lewis acid, imine **2** undergoes an intramolecular aza-Diels-Alder reaction, which can either occur concerted (Path A) or stepwise (Path B).¹⁰² The resulting tetrahydroquinoline **3** is then further oxidized to the quinoline product **4**. Lastly, reuse experiments were performed to ascertain the stability of **TpBpyCOF** in the reaction. Upon recycling the catalyst for five times, full conversion of the starting material was still achieved, however the yield had dropped to 45%, which is still 75% of the original activity (Figure S45). Moreover, while the main chemical linkages remained intact according to FTIR, the PXRD of the recycled material seemed to indicate that it had lost its crystallinity (Figure S46-47). The loss of activity and crystallinity, while unfortunate, has been observed many times for photoactive COFs, and can be attributed to photobleaching, partial deactivation by singlet oxygen and also possibly side reactions with intermediates formed during the reaction.^{39,45,103-105}

Table 4: Control experiments for the Povarov reaction.

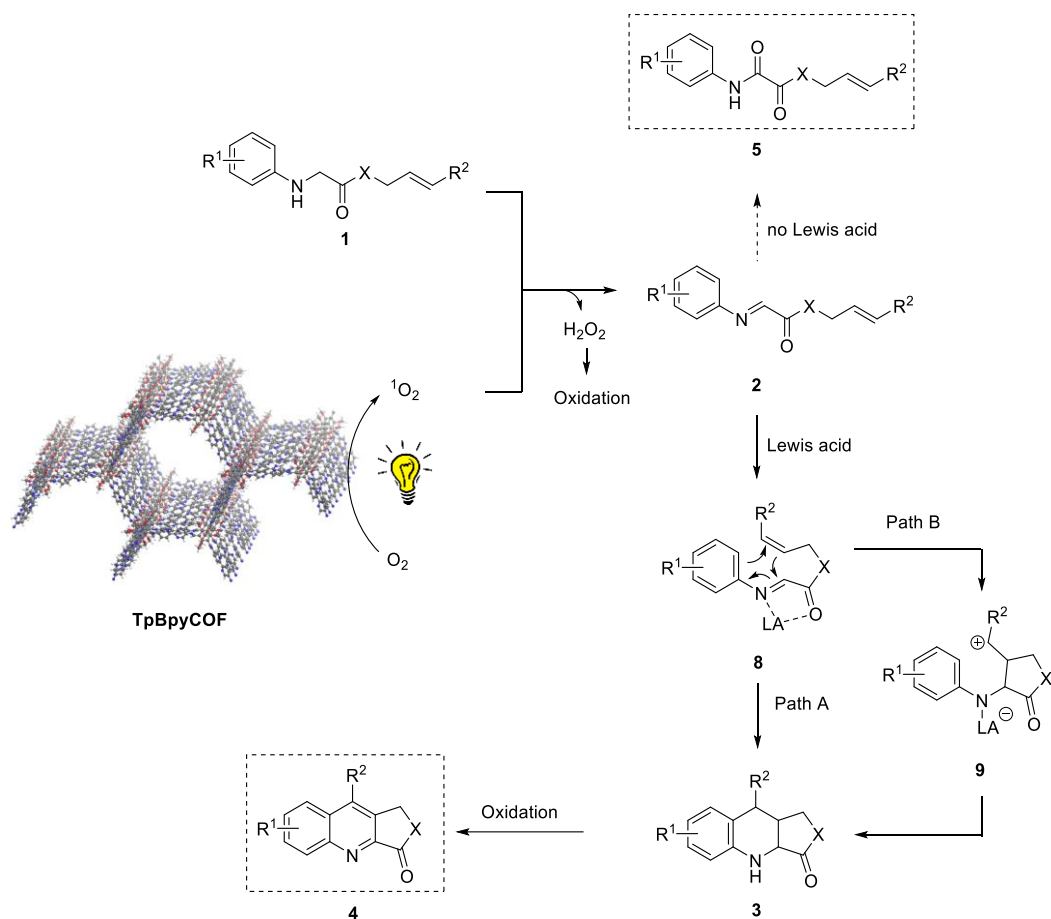
Entry	Conditions ^a	Result (%) ^b
1	No modification	62
2	In the dark	n.r. ^c
3	Under argon	n.r. ^c
4	No COF	n.r. ^c
5	No Lewis acid	42% 7a
6	<i>p</i> -Benzoquinone	52
7	Nitro blue tetrazolium chloride ^d	53
8	<i>i</i> PrOH	51
9	L-histidine	6
10	DABCO	n.r. ^c
11	NaN ₃	n.r. ^c
12	AgNO ₃	27
13	KI	n.r. ^c
14	TEMPO	10

^a Reaction conditions: 0.1 mmol cinnamyl *p*-tolylglycinate **1a**, 10 mg **TpBpyCOF**, 0.01 mmol Sc(OTf)₃, 0.1 mmol of quencher.

^b Determined by ¹H-NMR analysis using 1,3,5-trimethoxybenzene as an internal standard.

^c No reaction.

^d 0.015 mmol NBT.



Scheme 3: Mechanism for the photocatalytic generation of quinolines **4** and glyoxal derivatives **5** by **TpBpyCOF**.

CONCLUSIONS

In this work, two bipyridine- or phenylpyridine-based COFs, **TpBpyCOF** and **TpPpyCOF**, were successfully synthesized and photochemically characterized. The use of bipyridine led to a smaller band gap compared with phenylpyridine, and the resulting **TpBpyCOF** was a more effective photocatalyst. This work entailed the development of the first heterogeneous photocatalyst for the aerobic oxidation/Povarov cyclization and α -oxidation of *N*-aryl glycine derivatives, which are important transformations to generate highly substituted quinolines and dicarbonyl compounds. Using **TpBpyCOF** as a recyclable photocatalyst, a wide range of quinoline-fused lactones/lactams and glyoxal derivatives could be synthesized. The findings of our study expand the potential use of COFs in photocatalysis, hereby advancing the development of these novel materials as alternatives for homogeneous (metal-based) photocatalysts.

EXPERIMENTAL SECTION

General procedures

Unless stated otherwise all reagents and solvents were purchased from commercial sources and used without further purification. Dry tetrahydrofuran and dichloromethane were obtained using the MBraun SPS-800 solvent purification system. Dry *N,N*-dimethylformamide was obtained by drying over 4 Å molecular sieves and storing for at least two days prior to use. The synthesis of the building blocks for the COFs and the substrates for the aerobic oxidation/Povarov cyclization and α -oxidation of *N*-aryl glycine derivatives are described in the supporting information.

IR spectra of COFs and compounds were obtained in neat form with a Shimadzu IRAffinity1S WL FTIR spectrophotometer. Nitrogen adsorption-desorption isotherms were obtained using a Micromeritics® Tristar II. The samples were activated at 120 °C under vacuum overnight before measurements. Pore size distributions were calculated from N₂ sorption isotherms using quenched solid density functional theory (QSDFT) in ASiQwin. Powder X-ray diffraction (PXRD) spectra were taken using a Bruker D8 Advance spectrometer with a copper K α radiation source ($\lambda = 1.54056$ Å) at 40 kV and 45 mA with 1 °/s scanning speed. UV-Vis diffuse reflectance spectra were recorded in solid-state on a Perkin Elmer Lambda 1050 UV-Vis-NIR spectrophotometer. Photoelectrochemical measurements were performed in 0.2 M KCl/NaOH buffer (pH 12) or 0.06 M Na₂B₄O₇·10H₂O/NaOH buffer (pH 10) using an ALS-Japan Ag/AgCl 3 M NaCl reference electrode (+0.195 V vs. SHE), ALS-Japan Pt coil as counter electrode and the photocatalyst-coated FTO was used as working electrode. A Bio-Logic VSP potentiostat and EC-Lab software were used to record the measurements. White light was provided by a Philips Tornado T2 CFL (23 W, 1450 lumen). XPS was used to investigate the chemical composition of the surface of the materials, using the PHI 5000 VersaProbe II spectrometer. This was equipped with a monochromatic Al K α X-ray source ($h\nu = 1486.6$ eV) operating with a beam diameter of 200 μ m at 50 W. All measurements were taken using an angle of 45° between the beam and the sample and under a pressure of 10⁻⁶ Pa or less. The binding energies were calibrated with respect to the C-C/C-H peak of the C 1s spectrum at 285.0 eV. Survey scans and high-resolution spectra were analyzed using Multipak (v 9.6.1) software. The high-resolution spectra were deconvoluted as Gaussian-Lorentzian peaks to identify the corresponding chemical bonds. BF-TEM images were taken using a high contrast aperture (HCA) in bright-field mode on a JEOL JEM-2200FS TEM with a 200 kV field emission gun and the in-column energy filter (omega filter) at the UGent TEM Core Facility. The EPR spectra were recorded using a Bruker ESP300E spectrometer equipped with an HP 5350B microwave frequency counter and a Bruker NMR ERO35M gaussmeter. A microwave power of 20 mW was used. The field was modulated at a frequency of 100 kHz with an amplitude of 0.1-0.2 mT. The time constant was 2.56 ms and spectra were taken by an accumulation of 20 scans of 10s each. The magnetic fields were calibrated using the spectrum of diphenyl picryl hydrazyl ($g = 2.0036$). For the solid state EPR spectra a regular NMR tube was charged with 5 mg of the material. For spin trapping **TpBpyCOF** (3.75 mg) was stirred in 0.75 mL of a 200 mM spin trap solution (DMPO or TEMP) in CH₃CN, and illuminated for 10 minutes. The blanks were acquired by stirring the spin trap solution without COF for 10 minutes under visible light illumination. An aliquot of these suspensions was then used to charge 2 mm outer diameter and 1.4 mm inner diameter sample tubes, overfilling the full length of the rectangular EPR cavity, which was then directly measured in the EPR spectrometer in the case of spin trapping with DMPO. As commercial TEMP, even after distillation, contained significant amounts of TEMPO, and TEMPO radicals are stable, the samples were illuminated for a longer time (2 hours) and then the spectra were taken. Direct-excitation ¹H, ¹H-¹H Double Quantum - Single Quantum (DQ-SQ), ¹H-¹³C CPMAS and ¹H-¹³C CP-HETCOR spectra were acquired on a Bruker Avance Neo 800 MHz (18.8 T) spectrometer equipped with a 1.9mm H/X/Y triple resonance probehead. The sample was filled in a 1.9mm ZrO₂ rotor, and subjected to 35

kHz magic angle spinning (MAS). Prior to the insertion into the probe, the sample filled rotor was subjected to vacuum treatment (75 mTorr) at 353K. Direct-excitation (DE) ^1H (801.25 MHz) MAS NMR experiments were performed with an excitation pulse of 140 kHz radio-frequency (RF) field strength, accumulating 32 transients with a recycle delay of 3 s. 2D ^1H - ^1H double-quantum–single-quantum (DQ-SQ) correlation measurements were carried out using an excitation pulse of 140 kHz RF field strength, measured using the BABA sequence.¹⁰⁶ The two-dimensional spectra were collected with 80 t_e increments of 28.6 μs and 16 transients in the direct dimension. ^1H - ^{13}C CPMAS experiments were performed at a MAS rate of 35 kHz, using 12288 scans and a contact time of 1000 μs , a ^1H contact pulse of 120 kHz RF field strength (100-70% ramped pulse), a square pulse of 50 kHz RF field strength on ^{13}C and 60 kHz spin64 ^1H decoupling acquisition were used. ^1H - ^{13}C CP-HETCOR spectra were acquired with 400 scans in the direct dimension, 32 t_e increments of 28.57 μs . During acquisition, SPINAL64¹⁰⁷ ^1H decoupling was carried out, using a pulse of 60 kHz RF field strength. All the spectra were referenced to the adamantane ^1H resonance at 1.81 ppm and the ^{13}C (most downfield) resonance at 38.5 ppm, respectively. ^1H -NMR and ^{13}C -NMR spectra of solutions were recorded with a Bruker Avance III HD-400 spectrophotometer at 25 °C at 400 and 100 MHz, respectively. The NMR was equipped with 1H/BB z-gradient probe (BBO, 5 mm). All spectra were acquired through standard sequences available in the Bruker pulse program library and processed using TOPSPIN 4.1. An Agilent 1200 series HPLC system fitted with an Ascentis® Express C18 column (particle size 2.7 μm , length 30 mm, internal diameter 4.6 mm) was used for HPLC(-MS) using a mixture of acetonitrile/water (5 mM NH_4OAc) as the eluent. The HPLC was connected with a UV-Vis detector and an Agilent 1100 series LC/MSD-type SL mass spectrometer (ESI, 4000 V) using a mass-selective single quadrupole detector. Thin layer chromatography (TLC) for the analysis of reaction mixtures or gradient determination for chromatography was performed using glass-backed 0.25-mm Merck silica gel 60 F254 TLC plates, and visualized under UV light (254 nm). Column chromatography was performed with glass columns using silica gel (particle size 35-70 μm , pore diameter 6 nm) or on a Büchi Reveleris® X2 flash chromatography system (normal phase) or Grace Reveleris® X1 flash chromatography system (reversed phase), using prepacked Reveleris® silica or Reveleris® C18 cartridges.

Synthesis of COFs

The procedure to synthesize **TpBpyCOF** was modified from a literature procedure.⁴⁷ An Agilent GC vial (size: 22.75 mm x 75 mm; 20 mm cap) was charged with 1,3,5-triformylphloroglucinol **Tp** (63.0 mg, 0.3 mmol, 1 eq.) and 2,2'-bipyridine-5,5'-diamine **Bpy** (83.7 mg, 0.45 mmol, 1.5 eq.). Dimethylacetamide (DMAc, 4.5 mL) and *o*-dichlorobenzene (*o*DCB, 1.5 mL) were added via the sides of the vial, to flush the remaining solids from the walls. Then 0.6 mL of 6.0 M aqueous acetic acid was added and the vial was capped. This mixture was then sonicated for 10 minutes, flash frozen at 77 K in liquid N_2 and degassed by three freeze-pump-thaw cycles, after which the vial was put under argon. After warming to room temperature the vial was placed in an oven pre-heated at 120 °C. The resulting red powder was collected via filtration and washed sequentially with copious DMAc-DMF- H_2O -acetone-ethanol-THF. Further purification was done by Soxhlet extraction with methanol for 72 hours. Finally, the material was dried under vacuum overnight giving **TpBpyCOF** as a red powder (113 mg, 86%).

For **TpPpyCOF** the same procedure with **Ppy** (83 mg, 0.45 mmol, 1.5 eq.) and **Tp** (63.0 mg, 0.3 mmol, 1 eq.) was used, resulting in the title COF as an orange powder (103 mg, 79%).

General procedure for the aerobic oxidation/Povarov cyclization of *N*-aryl glycine derivatives

Typically, 20 mg **TpBpyCOF**, ScOTf_3 (10 mg, 0.02 mmol, 0.1 eq.), 0.2 mmol of substrate **1** and 2 mL CH_3CN were added to a small glass test tube. This was stirred under air and irradiated with a 26 W compact fluorescent lamp (CFL; ~10 cm distance) for 24 h. The reaction mixture was filtered over a

filter paper and washed with acetone. The filtrate was then evaporated and the product was purified using column chromatography (SiO₂, hexane/acetone: 10/1 or C18, gradient CH₃CN/H₂O: 30/70 – 100/0).*

*Reversed phase for **4c,e,h,k**.

General procedure for the α -oxidation of *N*-aryl glycine derivatives

Typically, 20 mg **TpBpyCOF**, 0.2 mmol of substrate **6** and 2 mL CH₃CN were added to a small glass test tube. This was stirred under air and irradiated with a 26 W CFL (~10 cm distance) for 24-36 h. The reaction mixture was filtered through a filter paper and rinsed thoroughly with acetone. The filtrate was then evaporated and the crude product was purified using column chromatography (C18, gradient CH₃CN/H₂O: 40/60 – 100/0 or 50/50 – 100/0).

Acknowledgements

The authors acknowledge the Research Board of Ghent University (BOF GOA20177000303) for funding. NMRCoRe (E.B & S.R) acknowledge the European Research Council (ERC) for an Advanced Research Grant under the European Union's Horizon 2020 research and innovation program under grant agreement No. 834134 (WATUSO). NMRCoRe acknowledges the Flemish government, department EWI for infrastructure investment via the Hermes Fund (AH.2016.134) and for financial support as International Research Infrastructure (I001321N: Nuclear Magnetic Resonance Spectroscopy Platform for Molecular Water Research).

REFERENCES

- (1) Wang, G.-B.; Li, S.; Yan, C.-X.; Zhu, F.-C.; Lin, Q.-Q.; Xie, K.-H.; Geng, Y.; Dong, Y.-B. Covalent organic frameworks: emerged high-performance platforms for efficient photocatalytic applications. *J. Mater. Chem. A* **2020**, *8*, 6975–6983.
- (2) Zhang, T.; Xing, G.; Chen, W.; Chen, L. Porous organic polymers: A promising platform for efficient photocatalysis. *Mater. Chem. Front.* **2020**, *4* (2), 332–353.
- (3) Romero, N. A.; Nicewicz, D. A. Organic Photoredox Catalysis. *Chem. Rev.* **2016**, *116* (17), 10075–10166.
- (4) Schultz, D. M.; Yoon, T. P. Solar synthesis: Prospects in visible light photocatalysis. *Science*. **2014**, p 1239176.
- (5) Koike, T.; Atika, M. Visible-light radical reaction designed by Ru- and Ir-based photoredox catalysis. *Inorg. Chem. Front.* **2014**, *1*, 562.
- (6) Teegardin, K.; Day, J. I.; Chan, J.; Weaver, J. Advances in Photocatalysis: A Microreview of Visible Light Mediated Ruthenium and Iridium Catalyzed Organic Transformations. *Org. Process. Res. Dev.* **2016**, *20* (7), 1156–1163.
- (7) Schilling, W.; Riemer, D.; Zhang, Y.; Hatami, N.; Das, S. Metal-Free catalyst for visible-light-induced oxidation of unactivated alcohols using Air/Oxygen as an oxidant. *ACS Catal.* **2018**, *8* (6), 5425–5430.
- (8) Xia, J. B.; Zhu, C.; Chen, C. Visible light-promoted metal-free C-H activation: Diarylketone-catalyzed selective benzylic mono- and difluorination. *J. Am. Chem. Soc.* **2013**, *135* (46), 17494–17500.
- (9) Joshi-Pangu, A.; Lévesque, F.; Roth, H. G.; Oliver, S. F.; Campeau, L. C.; Nicewicz, D.; DiRocco, D. A. Acridinium-Based Photocatalysts: A Sustainable Option in Photoredox Catalysis. *J. Org. Chem.* **2016**, *81* (16), 7244–7249.
- (10) Lee, S. H.; Nam, D. H.; Park, C. B. Screening xanthene dyes for visible light-driven nicotinamide adenine dinucleotide regeneration and photoenzymatic synthesis. *Adv. Synth. Catal.* **2009**, *351* (16), 2589–2594.
- (11) Ni, M.; Leung, M. K. H.; Leung, D. Y. C.; Sumathy, K. A review and recent developments in photocatalytic water-splitting using TiO₂ for hydrogen production. *Renew. Sust. Energ. Rev.* **2007**, *11* (3), 401–425.
- (12) Andrew Frame, F.; Carroll, E. C.; Larsen, D. S.; Sarahan, M.; Browning, N. D.; Osterloh, F. E. First demonstration of CdSe as a photocatalyst for hydrogen evolution from water under UV and visible light. *Chem. Commun.* **2008**, No. 19, 2206–2208.
- (13) Tahir, M. B.; Nabi, G.; Rafique, M.; Khalid, N. R. Nanostructured-based WO₃ photocatalysts: recent development, activity enhancement, perspectives and applications for wastewater treatment. *Int. J. Environ. Sci. Technol.* **2017**, *14* (11), 2519–2542.
- (14) Lee, G. J.; Wu, J. J. Recent developments in ZnS photocatalysts from synthesis to photocatalytic applications — A review. *Powder Technol.* **2017**, *318*, 8–22.

- (15) Ong, C. B.; Ng, L. Y.; Mohammad, A. W. A review of ZnO nanoparticles as solar photocatalysts: Synthesis, mechanisms and applications. *Renew. Sustain. Energy Rev.* **2018**, *81* (July 2016), 536–551.
- (16) Cao, S.; Low, J.; Yu, J.; Jaroniec, M. Polymeric Photocatalysts Based on Graphitic Carbon Nitride. *Adv. Mater.* **2015**, *27* (13), 2150–2176.
- (17) Wang, Y.; Wang, X.; Antonietti, M. Polymeric Graphitic Carbon Nitride as a Heterogeneous Organocatalyst : From Photochemistry to Multipurpose Catalysis to Sustainable Chemistry. *Angew. Chem. Int. Ed.* **2012**, 68–89.
- (18) Xiao, J. D.; Jiang, H. L. Metal-Organic Frameworks for Photocatalysis and Photothermal Catalysis. *Acc. Chem. Res.* **2019**, *52*, 356–366.
- (19) Dhakshinamoorthy, A.; Asiri, A. M.; García, H. Metal-Organic Framework (MOF) Compounds: Photocatalysts for Redox Reactions and Solar Fuel Production. *Angew. Chem. Int. Ed.* **2016**, *55* (18), 5414–5445.
- (20) Fan, H.; Mundstock, A.; Feldhoff, A.; Knebel, A.; Gu, J.; Meng, H.; Caro, J. Covalent Organic Framework-Covalent Organic Framework Bilayer Membranes for Highly Selective Gas Separation. *J. Am. Chem. Soc.* **2018**, *140* (32), 10094–10098.
- (21) Doonan, C. J.; Tranchemontagne, D. J.; Glover, T. G.; Hunt, J. R.; Yaghi, O. M. Exceptional ammonia uptake by a covalent organic framework. *Nat. Chem.* **2010**, *2* (3), 235–238.
- (22) Mulzer, C. R.; Shen, L.; Bisbey, R. P.; McKone, J. R.; Zhang, N.; Abruña, H. D.; Dichtel, W. R. Superior charge storage and power density of a conducting polymer-modified covalent organic framework. *ACS Cent. Sci.* **2016**, *2* (9), 667–673.
- (23) Halder, A.; Ghosh, M.; Khayum, A. M.; Bera, S.; Addicoat, M.; Sasmal, H. S.; Karak, S.; Kurungot, S.; Banerjee, R. Interlayer Hydrogen-Bonded Covalent Organic Frameworks as High-Performance Supercapacitors. *J. Am. Chem. Soc.* **2018**, *140* (35), 10941–10945.
- (24) Kaczmarek, A. M.; Liu, Y. Y.; Kaczmarek, M. K.; Liu, H.; Artizzu, F.; Carlos, L. D.; van der Voort, P. Developing Luminescent Ratiometric Thermometers Based on a Covalent Organic Framework (COF). *Angew. Chem. Int. Ed.* **2020**, *59* (5), 1932–1940.
- (25) Wu, X.; Han, X.; Xu, Q.; Liu, Y.; Yuan, C.; Yang, S.; Liu, Y.; Jiang, J.; Cui, Y. Chiral BINOL-Based Covalent Organic Frameworks for Enantioselective Sensing. *J. Am. Chem. Soc.* **2019**, *141* (17), 7081–7089.
- (26) Das, G.; Biswal, B. P.; Kandambeth, S.; Venkatesh, V.; Kaur, G.; Addicoat, M.; Heine, T.; Verma, S.; Banerjee, R. Chemical sensing in two dimensional porous covalent organic nanosheets. *Chem. Sci.* **2015**, *6* (7), 3931–3939.
- (27) Hu, H.; Yan, Q.; Ge, R.; Gao, Y. Covalent organic frameworks as heterogeneous catalysts. *Chinese J. Catal.* **2018**, *39* (7), 1167–1179.
- (28) Wu, Y.; Xu, H.; Chen, X.; Gao, J.; Jiang, D. A π -electronic covalent organic framework catalyst: π -walls as catalytic beds for Diels-Alder reactions under ambient conditions. *Chem. Commun.* **2015**, *51* (50), 10096–10098.
- (29) Liu, G.; Sheng, J.; Zhao, Y. Chiral covalent organic frameworks for asymmetric catalysis and chiral separation. *Sci. China. Chem.* **2017**, *60* (8), 1015–1022.

- (30) Gonçalves, R. S. B.; Deoliveira, A. B. V.; Sindra, H. C.; Archanjo, B. S.; Mendoza, M. E.; Carneiro, L. S. A.; Buarque, C. D.; Esteves, P. M. Heterogeneous Catalysis by Covalent Organic Frameworks (COF): Pd(OAc)₂@COF-300 in Cross-Coupling Reactions. *ChemCatChem* **2016**, *8* (4), 743–750.
- (31) Yan, X.; Liu, H.; Li, Y.; Chen, W.; Zhang, T.; Zhao, Z.; Xing, G.; Chen, L. Ultrastable Covalent Organic Frameworks via Self-Polycondensation of an A₂B₂ Monomer for Heterogeneous Photocatalysis. *Macromolecules* **2019**, *52*, 7977–7983.
- (32) Liu, W.; Su, Q.; Ju, P.; Guo, B.; Zhou, H.; Li, G.; Wu, Q. A Hydrazone-Based Covalent Organic Framework as an Efficient and Reusable Photocatalyst for the Cross-Dehydrogenative Coupling Reaction of N-Aryltetrahydroisoquinolines. *ChemSusChem* **2017**, *10* (4), 664–669.
- (33) Wei, P. F.; Qi, M. Z.; Wang, Z. P.; Ding, S. Y.; Yu, W.; Liu, Q.; Wang, L. K.; Wang, H. Z.; An, W. K.; Wang, W. Benzoxazole-Linked Ultrastable Covalent Organic Frameworks for Photocatalysis. *J. Am. Chem. Soc.* **2018**, *140* (13), 4623–4631.
- (34) Liu, H.; Li, C.; Li, H.; Ren, Y.; Chen, J.; Tang, J.; Yang, Q. Structural Engineering of Two-Dimensional Covalent Organic Frameworks for Visible-Light-Driven Organic Transformations. *ACS Appl. Mater. Interfaces*. **2020**, *12* (18), 20354–20365.
- (35) He, S.; Yin, B.; Niu, H.; Cai, Y. Targeted synthesis of visible-light-driven covalent organic framework photocatalyst via molecular design and precise construction. *Appl. Catal. B* **2018**, *239*, 147–153.
- (36) Sheng, J. L.; Dong, H.; Meng, X. bin; Tang, H. L.; Yao, Y. H.; Liu, D. Q.; Bai, L. L.; Zhang, F. M.; Wei, J. Z.; Sun, X. J. Effect of Different Functional Groups on Photocatalytic Hydrogen Evolution in Covalent-Organic Frameworks. *ChemCatChem* **2019**, *11* (9), 2313–2319.
- (37) Wang, Y.; Liu, H.; Pan, Q.; Wu, C.; Hao, W.; Xu, J.; Chen, R.; Liu, J.; Li, Z.; Zhao, Y. Construction of Fully Conjugated Covalent Organic Frameworks via Facile Linkage Conversion for Efficient Photoenzymatic Catalysis. *J. Am. Chem. Soc.* **2020**, *142* (13), 5958–5963.
- (38) Zhang, F.; Hao, H.; Dong, X.; Li, X.; Lang, X. Olefin-linked covalent organic framework nanotubes based on triazine for selective oxidation of sulfides with O₂ powered by blue light. *Appl. Catal. B* **2022**, *305*.
- (39) Liu, Z.; Yang, X.; Yang, Z.; Su, X.; Xie, Z.; Chen, W.; Zhang, W.; Chen, L. Quinacridone based 2D covalent organic frameworks as efficient photocatalysts for aerobic oxidative Povarov reaction. *Appl. Catal. B* **2022**, *312*.
- (40) Shi, J. L.; Chen, R.; Hao, H.; Wang, C.; Lang, X. 2D sp² Carbon-Conjugated Porphyrin Covalent Organic Framework for Cooperative Photocatalysis with TEMPO. *Angew. Chem. Int. Ed.* **2020**, *59* (23), 9088–9093.
- (41) Zhang, P.; Yin, Y.; Wang, Z.; Yu, C.; Zhu, Y.; Yan, D.; Liu, W.; Mai, Y. Porphyrin-Based Conjugated Microporous Polymer Tubes: Template-Free Synthesis and A Photocatalyst for Visible-Light-Driven Thiocyanation of Anilines. *Macromolecules* **2021**, *54* (7), 3543–3553.
- (42) Sun, N.; Wang, C.; Wang, H.; Gao, X.; Jiang, J. Photonic Switching Porous Organic Polymers toward Reversible Control of Heterogeneous Photocatalysis. *ACS Appl. Mater. Interfaces* **2020**, *12* (50), 56491–56498.

- (43) Li, S.; Li, L.; Li, Y.; Dai, L.; Liu, C.; Liu, Y.; Li, J.; Lv, J.; Li, P.; Wang, B. Fully Conjugated Donor-Acceptor Covalent Organic Frameworks for Photocatalytic Oxidative Amine Coupling and Thioamide Cyclization. *ACS Catal.* **2020**, *10* (15), 8717–8726.
- (44) Ayed, C.; Caire Da Silva, L.; Wang, D.; Zhang, K. A. I. Designing conjugated microporous polymers for visible light-promoted photocatalytic carbon-carbon double bond cleavage in aqueous medium. *J. Mater. Chem. A* **2018**, *6* (44), 22145–22151.
- (45) Zhang, K.; Kopetzki, D.; Seeberger, P. H.; Antonietti, M.; Vilela, F. Surface Area Control and Photocatalytic Activity of Conjugated Microporous Poly(benzothiadiazole) Networks. *Angew. Chem. Int. Ed.* **2013**, *125* (5), 1472–1476.
- (46) Li, R.; Ma, B. C.; Huang, W.; Wang, L.; Wang, D.; Lu, H.; Landfester, K.; Zhang, K. A. I. Photocatalytic Regioselective and Stereoselective [2 + 2] Cycloaddition of Styrene Derivatives Using a Heterogeneous Organic Photocatalyst. *ACS Catal.* **2017**, *7* (5), 3097–3101.
- (47) Shinde, D. B.; Aiyappa, H. B.; Bhadra, M.; Biswal, B. P.; Wadge, P.; Kandambeth, S.; Garai, B.; Kundu, T.; Kurungot, S.; Banerjee, R. A mechanochemically synthesized covalent organic framework as a proton-conducting solid electrolyte. *J. Mater. Chem. A* **2016**, *4* (7), 2682–2690.
- (48) Bhadra, M.; Sasmal, H. S.; Basu, A.; Midya, S. P.; Kandambeth, S.; Pachfule, P.; Balaraman, E.; Banerjee, R. Predesigned Metal-Anchored Building Block for in Situ Generation of Pd Nanoparticles in Porous Covalent Organic Framework: Application in Heterogeneous Tandem Catalysis. *ACS Appl. Mater. Interfaces* **2017**, *9* (15), 13785–13792.
- (49) Aiyappa, H. B.; Thote, J.; Shinde, D. B.; Banerjee, R.; Kurungot, S. Cobalt-Modified Covalent Organic Framework as a Robust Water Oxidation Electrocatalyst. *Chem. Mater.* **2016**, *28* (12), 4375–4379.
- (50) Cui, W.-R.; Zhang, C.-R.; Jiang, W.; Liang, R.-P.; Qiu, J.-D. Covalent Organic Framework Nanosheets for Fluorescence Sensing via Metal Coordination. *ACS Appl. Nano Mater.* **2019**, *2* (8), 5342–5349.
- (51) Kou, M.; Wang, Y.; Xu, Y.; Ye, L.; Huang, Y.; Jia, B.; Li, H.; Ren, J.; Deng, Y.; Chen, J.; Zhou, Y.; Lei, K.; Wang, L.; Liu, W.; Huang, H.; Ma, T. Molecularly Engineered Covalent Organic Frameworks for Hydrogen Peroxide Photosynthesis. *Angew. Chem. Int. Ed.* **2022**, *61* (19), e202200413.
- (52) Gofman, I. v.; Goikhman, M. Y.; Podeshvo, I. v.; Eliseeva, E. E.; Bol'Bat, E. E.; Abalov, I. v.; Yakimanskii, A. v. Films of polyamides with phenylpyridine units in the backbone. *Russ. J. Appl. Chem.* **2010**, *83* (10), 1862–1867.
- (53) Xia, A.; Guo, H.; Qiu, X.; Ding, M.; Gao, L. Syntheses and properties of polyimides derived from diamines containing 2,5-disubstituted pyridine group. *J. Appl. Polym. Sci.* **2006**, *102* (2), 1844–1851.
- (54) Halder, A.; Karak, S.; Addicoat, M.; Bera, S.; Chakraborty, A.; Kunjattu, S. H.; Pachfule, P.; Heine, T.; Banerjee, R. Ultrastable Imine-Based Covalent Organic Frameworks for Sulfuric Acid Recovery: An Effect of Interlayer Hydrogen Bonding. *Angew. Chem. Int. Ed.* **2018**, *57* (20), 5797–5802.

- (55) Li, R. L.; Yang, A.; Flanders, N. C.; Yeung, M. T.; Sheppard, D. T.; Dichtel, W. R. Two-Dimensional Covalent Organic Framework Solid Solutions. *J. Am. Chem. Soc.* **2021**, *143* (18), 7081–7087.
- (56) Mahmood, J.; Ahmad, I.; Jung, M.; Seo, J. M.; Yu, S. Y.; Noh, H. J.; Kim, Y. H.; Shin, H. J.; Baek, J. B. Two-dimensional amine and hydroxy functionalized fused aromatic covalent organic framework. *Commun. Chem.* **2020**, *3* (31).
- (57) Guo, J.; Xu, Y.; Jin, S.; Chen, L.; Kaji, T.; Honsho, Y.; Addicoat, M. A.; Kim, J.; Saeki, A.; Ihee, H.; Seki, S.; Irle, S.; Hiramoto, M.; Gao, J.; Jiang, D. Conjugated organic framework with three-dimensionally ordered stable structure and delocalized π clouds. *Nat. Commun.* **2013**, *4*, 2736.
- (58) Park, S. H.; Radhakrishnan, S.; Choi, W.; Chandran, C. V.; Kemp, K. C.; Breynaert, E.; Bell, R. G.; Kirschhock, C. E. A.; Hong, S. B. Hydrogen-Bonded Water-Aminium Assemblies for Synthesis of Zeotypes with Ordered Heteroatoms. *J. Am. Chem. Soc.* **2022**, *144* (39), 18054–18061.
- (59) Vallaey, B.; Radhakrishnan, S.; Heylen, S.; Chandran, C. V.; Taulelle, F.; Breynaert, E.; Martens, J. A. Reversible room temperature ammonia gas absorption in pore water of microporous silica-alumina for sensing applications. *Phys. Chem. Chem. Phys.* **2018**, *20* (19), 13528–13536.
- (60) Borgmans, S.; Rogge, S. M. J.; de Vos, J. S.; Stevens, C. v.; van der Voort, P.; van Speybroeck, V. Quantifying the Likelihood of Structural Models through a Dynamically Enhanced Powder X-Ray Diffraction Protocol. *Angew. Chem. Int. Ed.* **2021**, *60* (16), 8913–8922.
- (61) Stegbauer, L.; Zech, S.; Savasci, G.; Banerjee, T.; Podjaski, F.; Schwinghammer, K.; Ochsenfeld, C.; Lotsch, B. v. Tailor-Made Photoconductive Pyrene-Based Covalent Organic Frameworks for Visible-Light Driven Hydrogen Generation. *Adv. Ener. Mater.* **2018**, *8* (24).
- (62) Hankin, A.; Bedoya-Lora, F. E.; Alexander, J. C.; Regoutz, A.; Kelsall, G. H. Flat band potential determination: Avoiding the pitfalls. *J. Mater. Chem. A* **2019**, *7* (45), 26162–26176.
- (63) Cai, K.; Wang, W.; Zhang, J.; Chen, L.; Wang, L.; Zhu, X.; Yu, Z.; Wu, Z.; Zhou, H. Facile construction of olefin-linked covalent organic frameworks for enhanced photocatalytic organic transformation via wall surface engineering. *J. Mater. Chem. A* **2022**.
- (64) Liu, Z.; Su, Q.; Ju, P.; Li, X.; Li, G.; Wu, Q.; Yang, B. A hydrophilic covalent organic framework for photocatalytic oxidation of benzylamine in water. *Chem. Commun.* **2020**, *56* (5), 766–769.
- (65) Kabatc, J.; Kucybaia, Z.; Pietrzak, M.; Sigalski, F.; Paczkowski, J. Free radical polymerization initiated via photoinduced intermolecular electron transfer process: kinetic study 3. *Polymer (Guildf)* **1999**, *40*, 735–745.
- (66) Parrino, F.; D'Arienzo, M.; Mostoni, S.; Dirè, S.; Ceccato, R.; Bellardita, M.; Palmisano, L. Electron and Energy Transfer Mechanisms: The Double Nature of TiO₂ Heterogeneous Photocatalysis. *Top. Curr. Chem.* **2022**, *380* (1).
- (67) Bellardita, M.; Ceccato, R.; Dirè, S.; Loddo, V.; Palmisano, L.; Parrino, F. Energy Transfer in Heterogeneous Photocatalysis. *Subst. Int. J. Hist. Chem* **2019**, *3* (2), 49–57.
- (68) Ozawa, T.; Hanaki, A. Hydroxyl Radical produced by the Reaction of Superoxide Ion with Hydrogen Peroxide: Electron Spin Resonance Detection by Spin Trapping. *Chem. Pharm. bull.* **1978**, *26* (8), 2572–2575.

- (69) Wang, Z. J.; Ghasimi, S.; Landfester, K.; Zhang, K. A. I. Molecular Structural Design of Conjugated Microporous Poly(Benzooxadiazole) Networks for Enhanced Photocatalytic Activity with Visible Light. *Adv. Mater.* **2015**, *27* (40), 6265–6270.
- (70) Desrat, S.; van de Weghe, P. Intramolecular imino Diels - Alder reaction: Progress toward the synthesis of unciamycin. *J. Org. Chem.* **2009**, *74* (17), 6728–6734.
- (71) Nicolaou, K. C.; Chen, J. S.; Zhang, H.; Montero, A. Asymmetric Synthesis and Biological Properties of Unciamycin and 26-epi-Unciamycin. *Angew. Chem. Int. Ed.* **2008**, *120* (1), 191–195.
- (72) Nicolaou, K. C.; Zhang, H.; Chen, J. S.; Crawford, J. J.; Pasunoori, L. Total Synthesis and Stereochemistry of Unciamycin. *Angew. Chem. Int. Ed.* **2007**, *119* (25), 4788–4791.
- (73) Wang, H.; Ganesan, A. Total synthesis of the cytotoxic alkaloid luotonin A. *Tetrahedron Lett.* **1998**, *39* (49), 9097–9098.
- (74) Wall, M. E.; Wani, M. C.; Cook, C. E.; Palmer, K. H.; McPhail, A. T.; Sim, G. A. Plant Antitumor Agents. I. The Isolation and Structure of Camptothecin, a Novel Alkaloidal Leukemia and Tumor Inhibitor from *Camptotheca acuminata*. *J. Am. Chem. Soc.* **1966**, *88* (16), 3888–3890.
- (75) Anzini, M.; Cappelli, A.; Vomero, S.; Seeber, M.; Menziani, M. C.; Langer, T.; Hagen, B.; Manzoni, C.; Bourguignon, J. J. Mapping and fitting the peripheral benzodiazepine receptor binding site by carboxamide derivatives. Comparison of different approaches to quantitative ligand-receptor interaction modeling. *J. Med. Chem.* **2001**, *44* (8), 1134–1150.
- (76) Blair, A.; Zmuda, F.; Malviya, G.; Tavares, A. A. S.; Tamagnan, G. D.; Chalmers, A. J.; Dewar, D.; Pimlott, S. L.; Sutherland, A. A novel ¹⁸F-labelled high affinity agent for PET imaging of the translocator protein. *Chem. Sci.* **2015**, *6* (8), 4772–4777.
- (77) More, D. A.; Shinde, G. H.; Shaikh, A. C.; Muthukrishnan, M. Oxone promoted dehydrogenative Povarov cyclization of: N -aryl glycine derivatives: An approach towards quinoline fused lactones and lactams. *RSC Adv.* **2019**, *9* (52), 30277–30291.
- (78) Jia, X.; Peng, F.; Qing, C.; Huo, C.; Wang, X. Catalytic radical cation salt induced Csp³-H functionalization of glycine derivatives: Synthesis of substituted quinolines. *Org. Lett.* **2012**, *14* (15), 4030–4033.
- (79) Earle, M. J.; Vibert, A.; Jahn, U. Tris(4-bromophenyl)aminium Hexachloroantimonate. *Encyclopedia of Reagents for Organic Synthesis*; **2011**; Vol. 1, pp 1–6.
- (80) Dong, W.; Hu, B.; Gao, X.; Li, Y.; Xie, X.; Zhang, Z. Visible-Light-Induced Photocatalytic Aerobic Oxidation/Povarov Cyclization Reaction: Synthesis of Substituted Quinoline-Fused Lactones. *J. Org. Chem.* **2016**, *81* (19), 8770–8776.
- (81) Wang, J.; Li, L.; Guo, Y.; Li, S.; Wang, S.; Li, Y.; Zhang, Y. Visible-light-enabled aerobic oxidative Csp³-H functionalization of glycine derivatives using an organic photocatalyst: Access to substituted quinoline-2-carboxylates. *Org. Biomol. Chem.* **2020**, *18* (40), 8179–8185.
- (82) Cornel, V.; Lovely, C. J. Boron Trifluoride Etherate. *Encyclopedia of Reagents for Organic Synthesis*; **2007**; Vol. 2.

- (83) Fónagy, O.; Szabó-Bárdos, E.; Horváth, O. 1,4-Benzoquinone and 1,4-hydroquinone based determination of electron and superoxide radical formed in heterogeneous photocatalytic systems. *J. Photochem. Photobiol. A* **2021**, *407*, 113057.
- (84) Hyung, S. C.; Jun, W. K.; Cha, Y. N.; Kim, C. A quantitative nitroblue tetrazolium assay for determining intracellular superoxide anion production in phagocytic cells. *J. Immunoassay. Immunochem.* **2006**, *27* (1), 31–44.
- (85) Watts, R. J.; Teel, A. L. Hydroxyl radical and non-hydroxyl radical pathways for trichloroethylene and perchloroethylene degradation in catalyzed H₂O₂ propagation systems. *Water Res.* **2019**, *159*, 46–54.
- (86) Hartman, P. E.; Hartman, Z.; Ault, K. T. Scavenging of singlet molecular oxygen by imidazole compounds: high and sustained activities of carboxy terminal histidine dipeptides and exceptional activity of imidazole-4 acetic acid. *Photochem. Photobiol.* **1990**, *51* (1), 59–66.
- (87) Ouannes, C.; Wilson, T. Quenching of Singlet Oxygen by Tertiary Aliphatic Amines. Effect of DABCO. *J. Am. Chem. Soc.* **1968**, *90* (23), 6527–6528.
- (88) Saito, I.; Inoue, K.; Matsuura, T. Occurrence of the singlet-oxygen mechanism in photodynamic oxidations of guanosine. *Photochem. Photobiol.* **1975**, *21*, 27–30.
- (89) Rodríguez, E. M.; Márquez, G.; Tena, M.; Álvarez, P. M.; Beltrán, F. J. Determination of main species involved in the first steps of TiO₂ photocatalytic degradation of organics with the use of scavengers: The case of ofloxacin. *Appl. Catal. B* **2015**, *178*, 44–53.
- (90) Wang, Y.; Li, X.; Dong, X.; Zhang, F.; Lang, X. Triazine-based two dimensional porous materials for visible light-mediated oxidation of sulfides to sulfoxides with O₂. *J. Colloid Interface Sci.* **2022**, *616*, 846–857.
- (91) Bhadra, M.; Kandambeth, S.; Sahoo, M. K.; Addicoat, M.; Balaraman, E.; Banerjee, R. Triazine Functionalized Porous Covalent Organic Framework for Photo-organocatalytic E- Z Isomerization of Olefins. *J. Am. Chem. Soc.* **2019**, *141* (15), 6152–6156.
- (92) Zhu, S.; Rueping, M. Merging visible-light photoredox and Lewis acid catalysis for the functionalization and arylation of glycine derivatives and peptides. *Chem. Commun.* **2012**, *48* (98), 11960–11962.
- (93) Sun, N.; Jin, Y.; Wang, H.; Yu, B.; Wang, R.; Wu, H.; Zhou, W.; Jiang, J. Photoresponsive Covalent Organic Frameworks with Diarylethene Switch for Tunable Singlet Oxygen Generation. *Chem. Mater.* **2022**, *34* (4), 1956–1964.
- (94) Mojarrad, A. G.; Zakavi, S. Simple low cost porphyrinic photosensitizers for large scale chemoselective oxidation of sulfides to sulfoxides under green conditions: Targeted protonation of porphyrins. *Catal. Sci. Technol.* **2018**, *8* (3), 768–781.
- (95) Hao, W.; Chen, D.; Li, Y.; Yang, Z.; Xing, G.; Li, J.; Chen, L. Facile Synthesis of Porphyrin Based Covalent Organic Frameworks via an A₂B₂ Monomer for Highly Efficient Heterogeneous Catalysis. *Chem. Mater.* **2019**, 8100–8105.
- (96) Yang, F.; Chu, X.; Sun, J.; Zhang, Y.; Li, Z.; Liu, H.; Bai, L.; Qu, Y.; Jing, L. Efficient singlet oxygen generation by excitonic energy transfer on ultrathin g-C₃N₄ for selective photocatalytic oxidation of methyl-phenyl-sulfide with O₂. *Chin. Chem. Lett.* **2020**, *31* (10), 2784–2788.

- (97) Zhi, Y.; Li, K.; Xia, H.; Xue, M.; Mu, Y.; Liu, X. Robust porous organic polymers as efficient heterogeneous organo-photocatalysts for aerobic oxidation reactions. *J. Mater. Chem. A* **2017**, *5* (18), 8697–8704.
- (98) Saito, H.; Nosaka, Y. Mechanism of singlet oxygen generation in visible-light-induced photocatalysis of gold-nanoparticle-deposited titanium dioxide. *J. Phys. Chem. C* **2014**, *118* (29), 15656–15663.
- (99) Yamaguchi, T.; Sugiura, Y.; Yamaguchi, E.; Tada, N.; Itoh, A. Synthetic Method for the Preparation of Quinazolines by the Oxidation of Amines Using Singlet Oxygen. *Asian J. Org. Chem.* **2017**, *6* (4), 432–435.
- (100) Ushakov, D. B.; Plutschack, M. B.; Gilmore, K.; Seeberger, P. H. Factors influencing the regioselectivity of the oxidation of asymmetric secondary amines with singlet oxygen. *Chem. Eur. J.* **2015**, *21* (17), 6528–6534.
- (101) Jiang, G.; Chen, J.; Huang, J. S.; Che, C. M. Highly efficient oxidation of amines to imines by singlet oxygen and its application in ugi-type reactions. *Org. Lett.* **2009**, *11* (20), 4568–4571.
- (102) Hermitage, S.; Jay, D. A.; Whiting, A. Evidence for the non-concerted [4+2]-cycloaddition of N-aryl imines when acting as both dienophiles and dienes under Lewis acid-catalysed conditions. *Tetrahedron Lett.* **2002**, *43* (52), 9633–9636.
- (103) Traxler, M.; Gisbertz, S.; Pachfule, P.; Schmidt, J.; Roeser, J.; Reischauer, S.; Rabeah, J.; Pieber, B.; Thomas, A. Acridine Functionalized Covalent Organic Frameworks (COFs) as Photocatalysts for Metallaphotocatalytic C–N Cross-Coupling. *Angew. Chem. Int. Ed.* **2022**.
- (104) Zhang, F.; Li, X.; Dong, X.; Hao, H.; Lang, X. Microspheres for blue light photocatalytic selective oxidation of amines with O₂. *Chinese J. Catal.* **2022**, *43* (9), 2395–2404.
- (105) An, W.-K.; Zheng, S.-J.; Xu, X.; Liu, L.-J.; Ren, J.-S.; Fan, L.; Yang, Z.-K.; Ren, Y.; Xu, C. Integrating Benzofuran and Heteroradialene into Donor-Acceptor Covalent Organic Frameworks for Photocatalytic Construction of Multi-substituted Olefins. *Appl. Catal. B* **2022**, 121630.
- (106) Feike, M.; Demco, D. E.; Graf, R.; Gottwald, J.; Hafner, S.; Spiess, H. W. Broadband Multiple-Quantum NMR Spectroscopy. *J. Magn. Reson., Ser. A* **1996**, *122*, 214–221.
- (107) Bräuniger, T.; Wormald, P.; Hodgkinson, P. Improved proton decoupling in NMR spectroscopy of crystalline solids using the SPINAL-64 sequence. *Monatsh. Chem.* **2002**, *133* (12), 1549–1554.